



# Planetary chaos and inverted climate phasing in the Late Triassic of Greenland

Malte Mau<sup>a</sup>, Dennis V. Kent<sup>b,c,1</sup>, and Lars B. Clemmensen<sup>a,1</sup>

Edited by Jean Jouzel, Laboratoire des Sciences du Climat et de l'Environ, Orme des Merisiers, France; received October 13, 2021; accepted March 12, 2022

Sedimentological records provide the only accessible archive for unraveling Earth's orbital variations in the remote geological past. These variations modulate Earth's climate system and provide essential constraints on gravitational parameters used in solar system modeling. However, geologic documentation of midlatitude response to orbital climate forcing remains poorly resolved compared to that of the low-latitude tropics, especially before 50 Mya, the limit of reliable extrapolation from the present. Here, we compare the climate response to orbital variations in a Late Triassic midlatitude temperate setting in Jameson Land, East Greenland (~43°N paleolatitude) and the tropical low paleolatitude setting of the Newark Basin, with independent time horizons provided by common magnetostratigraphic boundaries whose timing has been corroborated by uranium-lead (U-Pb) zircon dating in correlative strata on the Colorado Plateau. An integrated cyclostratigraphic and magnetostratigraphic age model revealed long-term climate cycles with periods of 850,000 and 1,700,000 y ascribed to the Mars–Earth grand orbital cycles. This indicates a 2:1 resonance between modulation of orbital obliquity and eccentricity variations more than 200 Mya and whose periodicities are inconsistent with astronomical solutions and indicate chaotic diffusion of the solar system. Our findings also demonstrate antiphasing in climate response between low and midlatitudes that has implications for precise global correlation of geological records.

cyclostratigraphy | Milankovitch | lacustrine | Fleming Fjord Group

Modern astronomical solutions provide powerful tools for constructing high-precision geologic age models by tuning a cyclostratigraphic response to theoretical variations in insolation for eccentricity, obliquity, and precession (1). This has been demonstrated by cyclostratigraphic studies of the Cenozoic era revealing the presence of a marine-integrated response to astronomical cycles predicted by modern astronomical solutions (2). However, cyclostratigraphic records from geological ages beyond ~50 Mya cannot be calibrated to present astronomical solutions due to uncertainties created by numerical integration error and suspected chaotic behavior of the solar system (3). These uncertainties are especially reflected in the period of the two orbital grand cycles produced by the motions of Earth and Mars, the obliquity ( $s_4 - s_3$ ) and eccentricity ( $g_4 - g_3$ ) grand cycles (3), with present-day periods of 1.25 My and 2.45 My, respectively (4). During the last 30 My, Mars–Earth grand cycles have been in 2:1 secular resonance (3, 5). However, at some point in time prior to 50 Mya, modeling indicates that the inner planets of the Solar System experienced significant chaotic diffusion. This could result in a transformation of the 2:1 Mars–Earth resonance into either a new 1:1 resonance state or the same 2:1 resonance but with different periodicities (3, 6, 7). Geological evidence of these Mars–Earth cycles as long-term modulations of eccentricity and obliquity cycles is essential information to discriminate between various orbital solutions and to significantly improve the validity of these beyond ~50 Mya. This could pave the way for more precise geologic time scales, provide a better understanding of climate events that are thought to be forced by these long-term cycles (8–10), constrain the existence of additional past planets, and provide further tests of gravitational models (11).

The Jameson Land Basin in central East Greenland contains a well-exposed Late Triassic lacustrine succession in the Fleming Fjord Group that was situated at a ~43°N paleolatitude during Late Triassic times (Fig. 1A) (12, 13). The sediments contain a rich vertebrate fauna (14–20), which has been placed within a magnetostratigraphic context for global correlations and dating (13, 21). These lake deposits provide an orbitally paced midlatitude climate record, which enables the detection of eccentricity modulated precession as well as obliquity-paced signals. This permits the cyclostratigraphic record to uncover the full distribution of orbital cycles, including long-term

## Significance

Our study of climate response to orbital variations in a Late Triassic midlatitude temperate setting in Jameson Land, East Greenland, provides robust evidence of astronomically forced grand cycles ascribed to gravitational interactions between Earth and Mars and is an Early Mesozoic record where both Mars–Earth modulation components are present and constrained with adequate chronostratigraphic controls. These findings suggest chaotic behavior of the inner Solar System and have implications as reference points in calculations of the past motions of the planets in the Solar System. Furthermore, our findings demonstrate a climate antiphasing between low and midlatitudes, which has implications for precise correlation of geological records and for validating models of Earth's climate dynamics.

Author affiliations: <sup>a</sup>Department of Geosciences and Natural Resource Management, University of Copenhagen, Copenhagen K DK-1350, Denmark; <sup>b</sup>Lamont-Doherty Earth Observatory, Columbia University, Palisades, NY 10968; and <sup>c</sup>Earth and Planetary Sciences, Rutgers University, Piscataway, NJ 08854

Author contributions: M.M. and L.B.C. designed research; M.M., D.V.K., and L.B.C. performed research; M.M. and D.V.K. analyzed data; and M.M., D.V.K., and L.B.C. wrote the paper.

The authors declare no competing interest.

This article is a PNAS Direct Submission.

Copyright © 2022 the Author(s). Published by PNAS. This article is distributed under Creative Commons Attribution-NonCommercial-NoDerivatives License 4.0 (CC BY-NC-ND).

<sup>1</sup>To whom correspondence may be addressed. Email: [dvk@ldeo.columbia.edu](mailto:dvk@ldeo.columbia.edu) or [larsc@ign.ku.dk](mailto:larsc@ign.ku.dk).

This article contains supporting information online at <http://www.pnas.org/lookup/suppl/doi:10.1073/pnas.2118696119/-DCSupplemental>.

Published April 22, 2022.

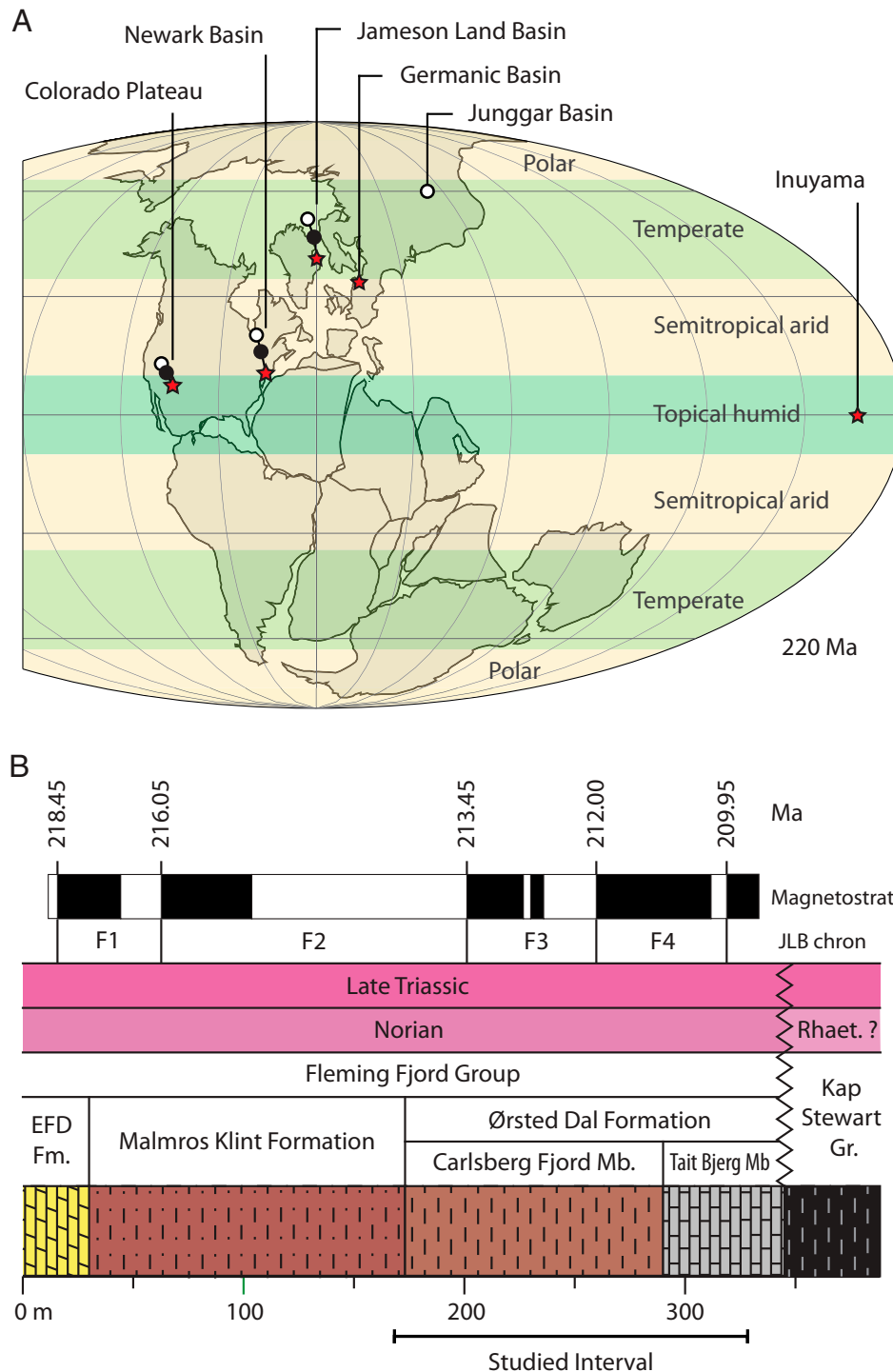


**Fig. 1.** Geologic setting of the Jameson Land Basin and some other Late Triassic basins mentioned in the text. (A) Paleogeographic reconstruction for 220 Mya of the Late Triassic (23) illustrating locations of the sedimentary basins mentioned in the text, where red stars are positions for 220 Mya, closed circles are positions for 210 Mya, and open circles are positions for 200 Mya. Generalized climate belts are from ref. 44. (B) Simplified stratigraphic log with magnetozones F1, F2, F3, and F4 from the Jameson Land Basin (JLB) (13) correlated to magnetochrons E13, E14, E15, and E16, respectively, from the N-H APTS that also provides the numerical age framework (23). The studied interval is indicated. EFD Fm., Edderfugledal Formation; JLB, Jameson Land Basin; Rhaet, Rhaetian; Magnetostrat, Magnetostratigraphy.

modulations of obliquity cycles, which are typically very weak in low-latitude tropical basins. The combination of magnetostratigraphy and cyclostratigraphy provides a powerful way to construct a high-precision age model for these ancient climate cycles whereby the geomagnetic polarity sequence has been calibrated with the stable long eccentricity (405 ky) metronome (22, 23). The resulting integrated age model allows for a precise record of the response to orbital variations in a midlatitude

temperate climate setting of the Jameson Land Basin that can be compared to the low-latitude setting of the Newark Basin linked with time horizons provided by common magnetostratigraphic boundaries. This study analyzes a 165-m-thick red bed succession in the upper part of the Fleming Fjord Group comprising the Carlsberg Fjord Member and lower half of the overlying Tait Bjerg Member of the Ørsted Dal Formation. The magnetostratigraphic correlation of this part of the Fleming

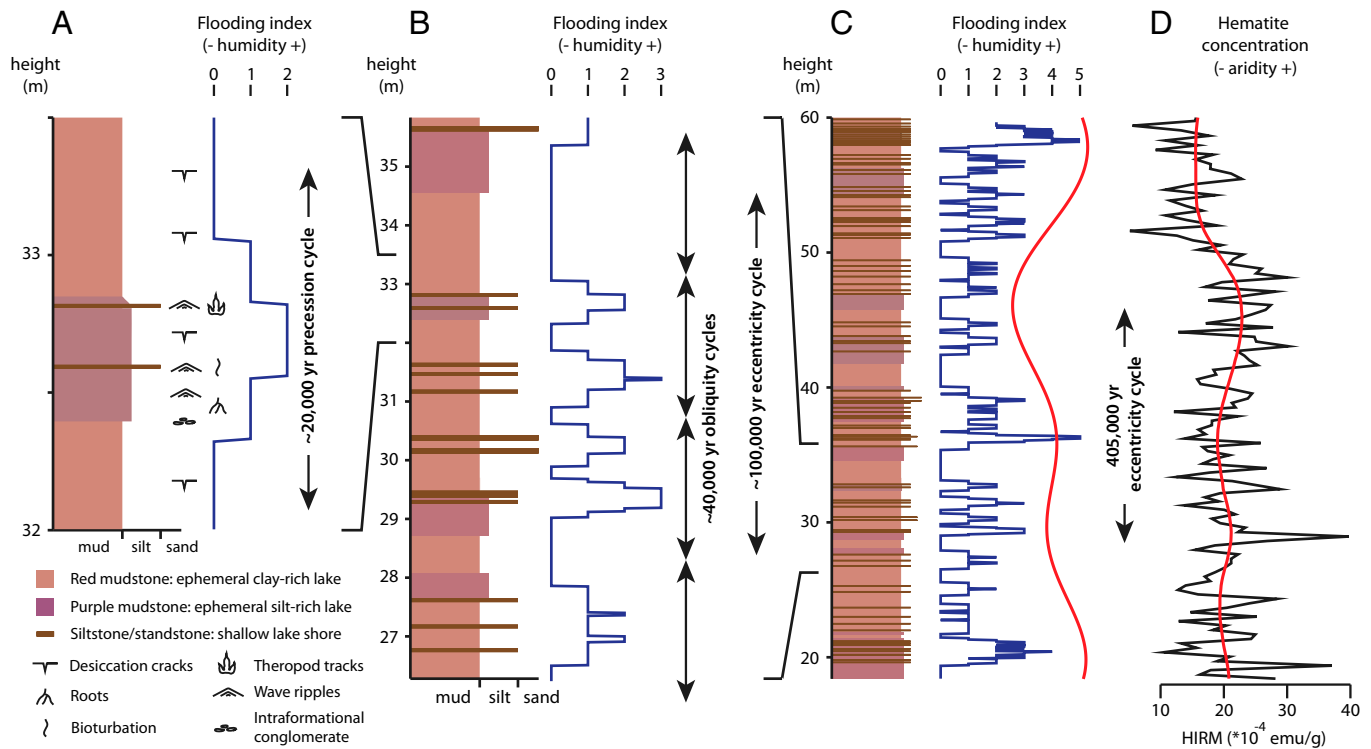


**Fig. 2.** Representative lithological cycles in the red bed secession of the Fleming Fjord Group based on field data from the lower part of the Carlsberg Fjord Member. (A) Basic meter-scale precessional cycle with typical sedimentary structures. (B) Obliquity cycles appear as alternating modifications of the precessional cycle. The short eccentricity cycle (100 ky) is expressed as bundling and amplitude modulation of around five basic precessional cycles. (C) The long eccentricity cycle (405 ky) expressed as bundling and amplitude modulation of basic precessional cycles. (D) Fluctuations in hematite concentration show higher aridity coinciding with a low FI and vice versa. Red lines are filtered signals (bandpass). Hard IRM fraction (HIRM) in c.g.s. electromagnetic units per gram. The FI is based on a simple moving average over a 0.5-m depth interval.

Fjord Group has been updated (13) to magnetochrons E14r to E17n of the Newark–Hartford astrochronostratigraphic polarity time scale (N-H APTS [23]), spanning an age of ~214 to 210 Mya in the Norian.

## Results

**Climate and Cyclostratigraphy.** A quasicyclic bedding has long been evident in exposures of the Fleming Fjord Group by color variation and the erosional profile (e.g., ref. 18). In the section of the Ørsted Dal Formation studied here, this variation is created by alternating red and purple mudstones, which are punctuated by centimeter-scale red to gray siltstone and sandstone beds. These red beds, corresponding to the Carlsberg Fjord Member, were deposited in a muddy ephemeral lake system (Fig. 1B). In the upper part of the studied succession corresponding to the Tait Bjerg Member, the sediments alternate between red beds and gray marlstone and limestone beds, interpreted as a more perennial lake system (12, 18). The mudstones are likely deposited from suspended material carried into the basin from the adjacent upland areas, with a possible minor input of wind-blown dust, including reworked soil aggregates (18, 24). The red mudstones are generally structureless but do contain desiccation cracks, whereas the purple mudstones are more coarse grained than the red mudstones and show occasional lamination, wave ripple marks, and plant roots (Fig. 2). Thus, the purple mudstones indicate periods with more humid climate and transport of more coarse-grained material to the basin. However, the mudstones represent a very ephemeral lacustrine environment with dominating mudflat deposition. Only during periods of increased precipitation did the water level in the basin increase sufficiently to allow short-lived transgressions of the former dry

mudflat and deposition of thin (<10 cm) wave-rippled siltstones and occasional sandstones reworked by wind-driven waves and deposited across the basin (25). The alternation between siltstones and mudstones is the greatest source of lithological variation in the Ørsted Dal Formation. The occurrence of siltstone and sandstone beds displays a cyclic bundling in the form of spacing/frequency and bed thicknesses (Fig. 2). Thus, a higher frequency of siltstone and sandstone beds represents periods with more frequent humid climate and lake highstand. This is quantified by generating a flooding index (FI) that represents the frequency of siltstone beds calculated as a simple moving average over a specific distance or time interval (*Materials and Methods*). The use of the FI as a lithological humidity proxy is supported by hematite fluctuations used as an aridity proxy (Fig. 2) and additional climate proxies (*SI Dataset*).

The lithological series reveal cyclic climate variations of the sedimentary and environmental characteristics of the lake system that are similar to the very shallow lake setting in the contemporaneous part of the Newark Basin section (26). In the case of the Fleming Fjord cyclicity, shown diagrammatically for the lower part of the studied section in Fig. 2, the basic meter-scale lithological cycles are interpreted as combinations of precessional and obliquity cycles of Earth's rotation axis, where the precessional cycles tend to be bundled in what can be interpreted as modulation by ~100-ky orbital eccentricity cycles and further in a ~18-m cycle corresponding to the 405-ky-long eccentricity modulation cycle. This interpretation is supported by statistical analysis of several climate proxies (*SI Dataset*). A comparable pattern of nested lithologic cycles containing similar orbital period ratios is also recognized in Norian playa deposits in the Germanic Basin (27) (Fig. 1A). However, the precession and obliquity cycles are poorly developed in the

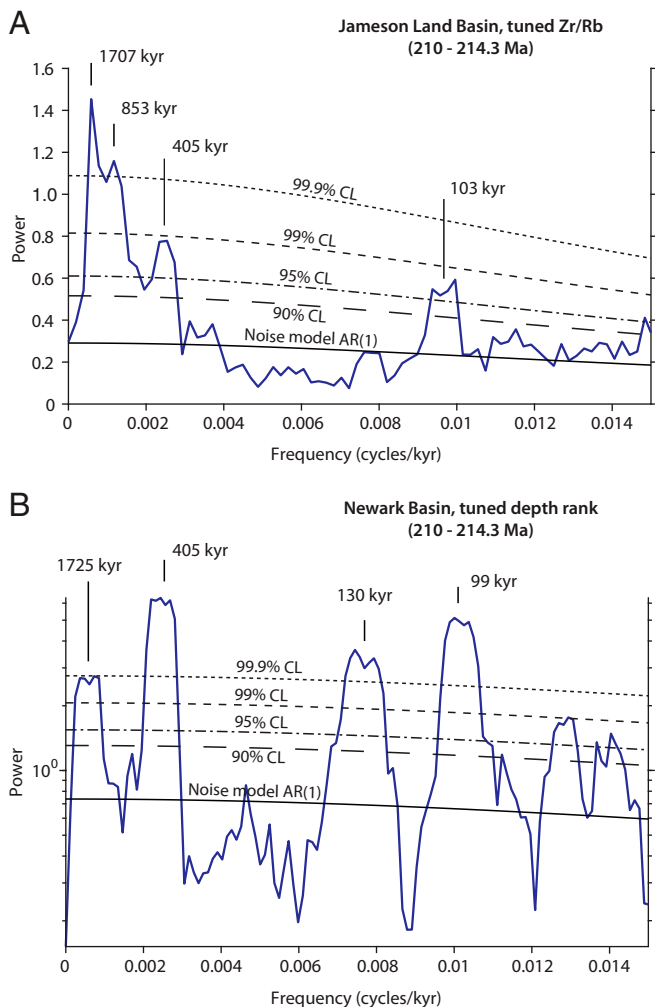


**Fig. 3.** Comparison of Thompson MTM analyses of the age-equivalent Jameson Land Basin and the Newark Basin climate records. (A) MTM spectrum of the zirconium/rubidium (Zr/Rb) record tuned to magnetostratigraphic chrons and the 405-ky metronome. The power spectrum from the Jameson Land Basin section shows a 103-ky cycle and a 405-ky cycle (approximation of 405 ky used in correlative N-H APTS) corresponding to short and long eccentricity. Furthermore, an 853-ky cycle and a 1,707-ky cycle corresponding to the two Mars–Earth grand cycles ( $s_4 - s_3$  and  $g_4 - g_3$ , respectively) are present. (B) The power spectrum from the age equivalent but higher resolution record of depth rank from Newark Basin section (11) shows a 99-ky cycle and a 130.3-ky cycle corresponding to short eccentricity. The 405-ky peak corresponds to the long eccentricity cycle (which was used for tuning the section), while the 1,725-ky cycle corresponds to the eccentricity modulating Mars–Earth cycle ( $g_4 - g_3$ ). CL, confidence level; AR, autoregressive.

Jameson Land Basin record, smeared and shifted to somewhat lower frequencies than predicted by astronomical solutions. This is most likely due to accumulation rate variability and a limited sampling rate in a relatively low-resolution record overall (SI Dataset) but not uncommonly found in statistical analyses of ancient lacustrine deposits (26, 28). Even in the thick lacustrine deposits of the Eocene Green River Formation, which could be considered a more recent analog of the Jameson Land Basin situated in a similar temperate belt setting in a high greenhouse world (29, 30), obliquity cyclicity has a weak lithologic expression (31) even though its contribution has been confirmed by formal multitaper method (MTM) spectral analysis (32).

**Long-Term Climate Cycles.** More clearly expressed in statistical tests and filtering of the Jameson Land Basin record are two long-term cycles with periods of 853 ky and 1,707 ky with respect to the interpreted 405-ky peak in the power spectral

density (PSD) plot (Fig. 3) and that are readily filtered from the FI record (Fig. 4). The 1,707-ky cycle closely matches a long-term cycle of similar periodicity ( $\sim 1,725$  ky) found in the Late Triassic record of the Newark Basin and most probably corresponds to the Mars–Earth eccentricity grand cycle ( $g_4 - g_3$ ) (11). In fact, this  $\sim 1,700$ -ky cycle is noticeably expressed as a long-term amplitude and frequency modulation of the 405-ky signal in both geochemical and lithological records in the Jameson Land Basin, as expected for the  $g_4 - g_3$  term (3). The obliquity grand cycle ( $s_4 - s_3$ ) has yet to be convincingly corroborated in the contemporaneous low-paleolatitude Newark record but might be expected in the higher-latitude Jameson Land Basin record, which contains a discernable obliquity signal. Indeed, comparison between spectral analyses of the 210.0- to 214.3-My interval corresponding to the studied succession reveals that no significant signal is present at a  $\sim 850$ -ky period in between the much weaker 923-ky and 720-ky eccentricity cycles identified in the Newark Basin (11), even though both the Jameson Land record and corresponding interval of the Newark record a prominent  $\sim 1,700$ -ky cycle (Fig. 3). Furthermore, comparisons of filtered  $\sim 40$ -ky obliquity cycles and  $\sim 850$ -ky cycles in the Jameson Land Basin indicate that the obliquity cycle is amplitude modulated by the  $\sim 850$ -ky cycle (SI Dataset). We are thus confident in interpreting the 850-ky cycle found in the Jameson Land Basin as reflecting the obliquity modulating grand cycle ( $s_4 - s_3$ ).

**Mid- Versus Low-Latitude Orbital Phases.** Magnetostratigraphic anchoring of the orbitally paced climate cycles in the Jameson Land Basin enables a comparison of relative phase and amplitude relationships with forcing from known 405-ky eccentricity modulation in the Newark Basin. The Jameson Land Basin record is converted from depth domain to time domain by tuning the depth record to the 405-ky metronome and magnetostratigraphic boundaries correlated with the Newark Basin (SI Dataset). Correlation of the tuned FI with the Newark Basin depth rank reveals that the humid peaks of the 405-ky-long eccentricity cycle ( $g_2 - g_5$ ) as well as the  $\sim 1,700$ -ky grand eccentricity cycle ( $g_4 - g_3$ ) are about  $180^\circ$  out of phase between the basins (Fig. 4). In the Jameson Land Basin, intervals with a high frequency of major lake flooding (higher FI), coarser grain sizes (higher Zr/Rb), and less hematite (lower hard isothermal remanent magnetization [HIRM]) correlate with a low depth rank (i.e., lake low stand) in the Newark Basin. Thus, when the Jameson Land Basin was in a humid climate phase, the Newark Basin was in an arid climate phase and vice versa. The antiphasing between the basins is clearly seen at common magnetostratigraphic boundaries. For example, an FI peak (humid climate peak) at magnetic polarity boundary between magnetozones F2r and F3n in the midlatitude Jameson Land Basin corresponds to a low in-lake depth index (more arid climate) at correlative chron boundary E14r/E15n in the low-latitude Newark Basin (Fig. 4). In the same way, FI troughs at magnetic polarity boundaries F3n/F3r and F3r/F4n at midlatitude Jameson Land correspond to lake level peaks at correlative chron boundaries E15n/E15r and E15r/E16n at low-latitude Newark. These magnetostratigraphic boundaries are considered globally synchronous time horizons (33) and provide a unique framework for spatiotemporal mapping of climate cycles.

## Discussion

**Implications for Earth and Solar System Modeling.** Grand cycles longer than 405 ky have been recognized in several Late

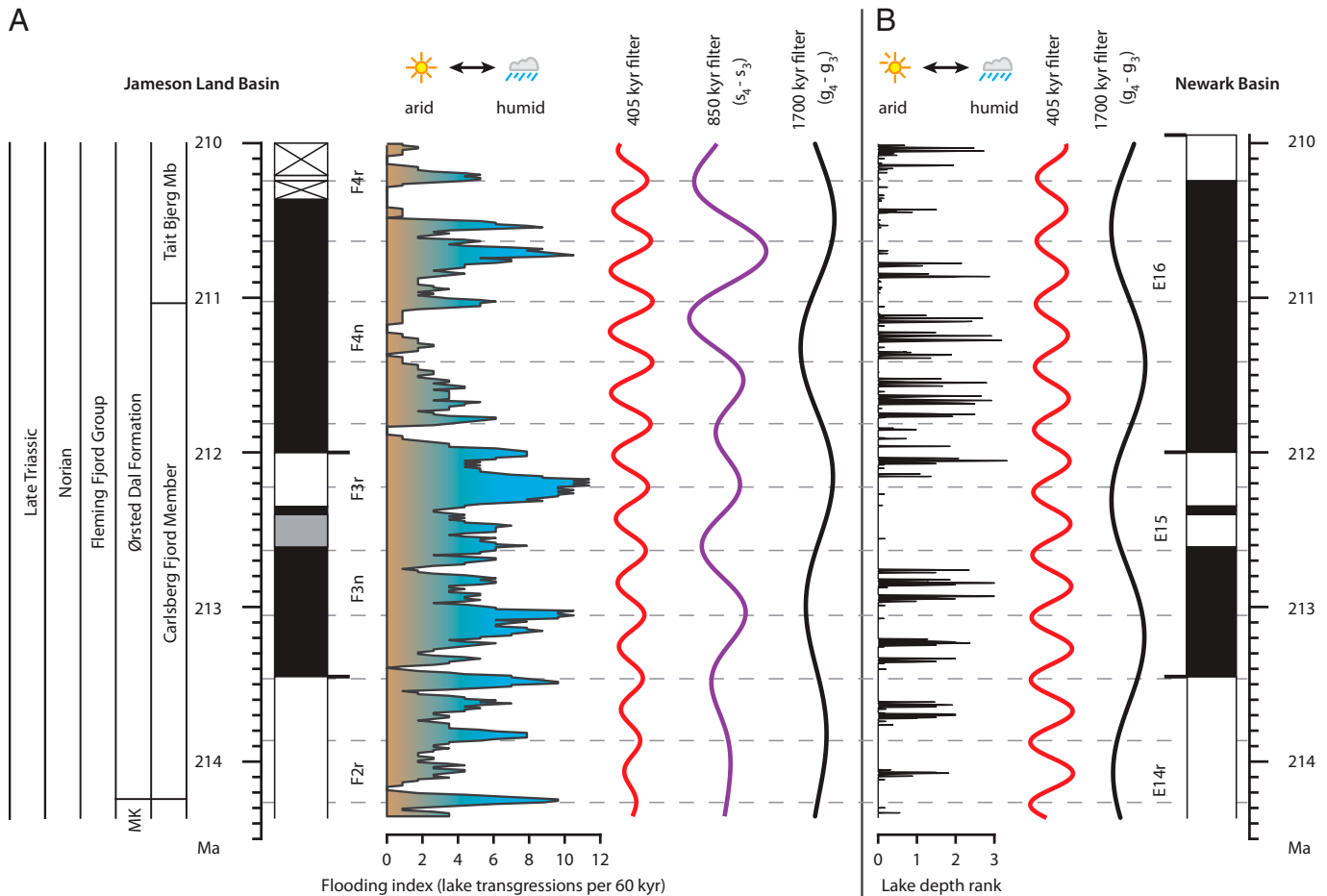


**Fig. 4.** Comparison of the timing of filtered low-frequency cycles in contemporaneous intervals from the Jameson Land Basin and the Newark Basin. (A) Data from the Jameson Land Basin (this study). (B) Data from the Newark Basin (11). The red filters represent the 405-ky cycle and are constructed with a bandpass filter range of 360 to 440 ky. The purple filter represents the 850-ky cycle and is constructed with a bandpass filter range of 700 to 1,200 ky. The black filters represent the  $\sim 1,700$ -ky cycle and are constructed with a bandpass filter range of 1,400 to 2,000 ky. The FI is based on a simple moving average over a 60-ky time interval. Crossed areas in the polarity record mark intervals with poor data, while the gray area marks an interval with poor paleomagnetic data and possible missing evidence for a reversed polarity chron. This reversed chron is exposed in other magnetostratigraphic records of the Fleming Fjord Group (13) and represents a very short depth interval.

Triassic successions. A 1,725-ky eccentricity modulating grand cycle was found in the Newark Basin (11), and virtually the same cycle (with a reported period of 1,800 ky) was identified in marine cherts in the Inuyama area in present-day Japan (34). This suggests a shift of the modern 2,450-ky cycle (4) to a period of 1,700 to 1,800 ky in the Late Triassic. However, the obliquity modulating grand cycle has not been observed in either the Newark Basin or the Inuyama area most probably due to their low latitude depositional environments where insolation changes from obliquity forcing are expected to be minimal. A hint of a long ( $\sim 820$ -ky) obliquity modulating grand cycle was reported in a study of the high-latitude Late Triassic–Early Jurassic Junggar Basin section (27), although the record was characterized (11) as lacking an independent geochronology or paleomagnetic polarity record for correlation. Thus, none of the previous Late Triassic studies have been able to adequately constrain the obliquity modulating grand cycle for comparison to the eccentricity grand cycle in the same or time-correlative record, which is, in theory, possible in mid- to high-latitude records (3, 35).

The shift of the  $g_4 - g_3$  component from the present-day 2,450-ky period to a  $\sim 1,700$ -ky period and the concomitant shift of the  $s_4 - s_3$  component from the present-day 1,250-ky period to an  $\sim 850$ -ky period are inconsistent with astronomical

solutions and provide direct evidence of the chaotic behavior of the inner planets of the solar system. The periods found in this study result in a 2:1 Mars–Earth resonance state, which is identical to the present-day 2:1 ratio of eccentricity to inclination. Thus, although some solar system modeling suggests a transition to the modern 2:1 ratio from a 1:1 resonance state sometime before the limit of computational extrapolation at 50 Mya and a Cretaceous ( $\sim 90$  Mya) sequence that offers tantalizing evidence of a 1:1 resonance state (36), our evidence from the  $\sim 214$ - to 210-Mya record in the Jameson Land Basin shows that a 2:1 resonance state prevailed in the Late Triassic and implies that one or more additional transitions in resonance state occurred in the intervening time interval. The results from our study provide a constraint for Solar System chaos and Mars–Earth secular resonance for  $\sim 214.4$  to 210 Mya, which can be used as a reference point in future astronomical solutions for the Late Triassic.

An unexpected finding in our study is the inverted climate response to eccentricity cycles in the midlatitude Jameson Land Basin compared to the low-latitude Newark Basin whereby the filtered  $\sim 1,700$ -ky cycle is remarkably anticorrelated with the filtered  $\sim 1,700$ -ky cycle in the Newark Basin, just like the climate response to the 405-ky cycle that anticorrelates between the basins (Fig. 4). The phase parallelism of the 405-ky

metronome and the  $\sim 1,700$ -ky grand cycle supports their correct identification. Recognizing that the Jameson Land Basin record is from the temperate humid belt whereas the correlative portion of the Newark Basin record is  $\sim 30^\circ$  closer to the equator from the semitropical arid belt (Fig. 1A), we can attempt to explain the latitudinal inversion of eccentricity insolation forcing by analogy with latitudinal differences in climate response to changing atmospheric  $\text{CO}_2$  concentration in general circulation models (37). As atmospheric  $\text{CO}_2$  concentration increases, such modeling experiments show a decrease in net moisture or runoff (i.e., reduced precipitation minus evaporation [ $P - E$ ]) in the semitropical arid belt but an increase in  $P - E$  in the bounding temperate and equatorial humid belts related to intensification of the Hadley cell. Pending testing with global climate modeling, we suggest that the latitudinal pattern of change in  $P - E$  with greenhouse climate forcing may be similar to change in insolation forcing from eccentricity whereby the climate response ( $P - E$ ) will be opposite in the semitropical arid belt (Newark Basin) and temperate humid belt (Jameson Land Basin), as indicated by the empirical data. General circulation models also show that obliquity-driven insolation creates increased poleward moisture transport in temperate latitudes during Northern Hemisphere summer at low tilt angles (38, 39). Although not expected to influence correlation of the temperate latitude Jameson Land Basin record with the subtropical Newark Basin record, which does not have an obliquity signal, climate antiphasing from obliquity forcing could potentially be produced with respect to lacustrine and fluvial records from polar latitudes, such as the Junggar Basin. We conclude that climate belts are an important consideration when correlating cyclostratigraphic records across latitudes, as they might show inverted climate phase response, which if not realized could produce significant temporal offsets (e.g.,  $\sim 200$  ky in the case of the 405-ky eccentricity cycle). This could have important implications for detailed age control based on correlation using cyclostratigraphy and the astrochronostratigraphic polarity time scale (23).

All lithostratigraphic subunits in the Fleming Fjord Group display a quasicyclic bedding that is most probably orbitally forced (18). Thus, the 160-m cyclostratigraphic record presented in this study has the potential to be eventually extended to a 300- to 400-m-thick succession that represents the entire Fleming Fjord Group and a time span of about 11 My (13). Such an extended record would provide more secure context for analysis of long-term climate cycles (11) and could further validate the Mars–Earth orbital cycles we already see imprinted in the upper part of the Fleming Fjord Group. Several localities along the western shore of the Carlsberg Fjord have optimal exposure conditions for field studies of most of the Fleming Fjord Group. In particular, Tait Bjerg would be a well-suited study site since paleomagnetic data have already been published in the Carlsberg Fjord Member and the Malmros Klint Formation at this locality (13). Another desired improvement would be more closely spaced measurements of lithofacies and elemental compositions, which could be done at selected sites with continuous, clean, and well-exposed cliff or ravine sections in the Edderfugledal and Malmros Klint Formations; this would allow better resolution of short-period precession and obliquity cycles now obscured by relatively coarse sampling intervals. Ultimately, a continental scientific coring project targeting complete recovery of the Fleming Fjord Group would be the most optimal method for enhancing this unique temperate latitude cyclic record for the Late Triassic.

## Materials and Methods

**Rock Sample Analyses.** Each locality was sampled for cyclostratigraphic analysis every 33 to 35 cm, resulting in a Nyquist wavelength of  $\sim 70$  cm. Samples for paleomagnetic analyses were collected every 1.75 m. All samples were collected from fresh sediments in pits dug centimeters to decimeters below the surface. Samples collected for cyclostratigraphic analysis were rinsed with demineralized water, dried at  $50^\circ\text{C}$ , and crushed with a vibratory ball mill before analysis. X-ray fluorescence (XRF) analyses were performed with a fixed Olympus Delta Premium DP-6000 XRF analyzer at the Department of Geosciences and Natural Resource Management XRF laboratory (University of Copenhagen). Each sample was analyzed for  $2 \times 120$  s with a 10-kV beam and a 30-kV beam. The crushed samples were covered with thin Mylar film to improve the detection limit of the lightest elements. The accuracy was regularly tested by reanalyzing samples and by analyzing the marine sediment certified reference material PACS-3 and pure  $\text{SiO}_2$ . Color analyses were performed with a Voltcraft plus RGB-2000 color analysis device on crushed bulk samples through thin film. The measured 10-bit red-green-blue (RGB) values provide a resolution of 1,024 shades of each primary color. The RGB color space was converted to the International Commission on Illumination  $L^*a^*b^*$  (CIELAB) color space with the `rgb2lab` function in Matlab. The entire Carlsberg Fjord Member was sampled for magnetostratigraphy in 2018. The same paleomagnetic field sampling, laboratory, and analytical procedures were followed as for the 1992 and 1995 sample sets as described previously (13, 21). This basically involved complete progressive thermal demagnetization in 12 or more steps to  $680^\circ\text{C}$  to isolate components of natural remanent magnetization in the oriented samples. For remanent coercivity analysis, the isothermal remanent magnetization (IRM) of sample chips were measured after being subjected to a 1-T magnetic field pulse. The samples were then remeasured after exposure to a 300-mT backfield to gauge the contribution from lower coercivity magnetite and maghemite. The magnetically hard IRM fraction (HIRM) attributable to hematite was calculated with  $0.5 \times (\text{IRM}_{+1\text{T}} + \text{IRM}_{-300\text{mT}})$ . IRM were produced with an ASC Scientific model IM-10-30 impulse magnetizer; thermal demagnetizations were done in an ASC Scientific TD48 oven, and all sample remanences were measured in a 2G, Inc. model 760 3-axis DC SQUID magnetometer housed in a magnetically shielded room at the LDEO Paleomagnetism Laboratory.

**Signal Processing.** All PSD plots were estimated with the Thomson MTM (40) using the “`pmtm`” function from the signal processing toolbox in Matlab. The time-bandwidth product (NW) was set to 2. The number of tapers used to calculate the PSD was by default  $2 \times \text{NW} - 1$ , resulting in three tapers. The fast Fourier transform was set to the next power of 2 greater than the length of the dataset. To remove unwanted effects caused by other factors than orbital cycles, the datasets were detrended before the MTM analysis by removing the best linear fit. MTM confidence levels were estimated with the robust autoregressive noise model AR1 (41). The evolutionary wavelet spectrum was computed with a Morlet wavelet with the Matlab script of ref. 42. Bandpass filters were constructed with the `bandpass` function from the signal processing toolbox in Matlab to extract cycles from the data. The Astronchron package in R (43) was used to tune the dataset to specified time points (the 405-ky metronome and magnetostratigraphic boundaries; [SI Dataset](#)) and interpolate the tuned stratigraphic series onto an evenly spaced data grid of one data point per 5 ky.

**Construction of the FI.** Climate-sensitive lithological data were quantified by generating a FI, which represents the frequency of siltstone beds throughout the lake succession. The FI was calculated as the simple moving average of the siltstone bed concentration over a specified depth or time interval. The moving average FI in Fig. 2 was created before tuning to the age model by adding all siltstone beds within a 0.5-m stratigraphic range to resolve the lithological cycles at decimeter scale. The moving average FI in Fig. 4 was created after tuning to the age model by adding all siltstone beds within a 60-ky time range to resolve the long-term lithological cycles.

**Data Availability.** All study data are included in the article and/or supporting information.

**ACKNOWLEDGMENTS.** We thank the Independent Research Fund Denmark for funding this project, the Geologic Survey of Denmark and Greenland for

logistical help in the field, and the Paleomagnetic Research Fund at Lamont-Doherty Earth Observatory for the magnetostratigraphic work. We also thank Paul Olsen for helpful comments and suggestions to the manuscript, Jesper Milan for taking drone photos of the outcrops, Nicolai Frobøse for sampling

and laboratory analyses of samples from the Tait Bjerg Member, and Christian Bjerrum for access to XRF equipment and for advice regarding sample collection for cyclostratigraphy. We would also like to thank two anonymous reviewers for constructive comments that helped us to improve the revised paper.

1. K. P. Kodama, L. A. Hinnov, *Rock Magnetic Cyclostratigraphy* (John Wiley & Sons, vol. 5, 2015)
2. T. Westerhold *et al.*, An astronomically dated record of Earth's climate and its predictability over the last 66 million years. *Science* **369**, 1383–1387 (2020).
3. J. Laskar, A. Fienga, M. Gastineau, H. Manche, La2010: A new orbital solution for the long-term motion of the Earth. *Astron. Astrophys.* **532**, A89 (2011).
4. L. A. Hinnov, New perspectives on orbitally forced stratigraphy. *Annu. Rev. Earth Planet. Sci.* **28**, 419–475 (2000).
5. H. Pälike, J. Laskar, N. J. Shackleton, Geologic constraints on the chaotic diffusion of the solar system. *Geology* **32**, 929–932 (2004).
6. J. Laskar, The chaotic motion of the solar system: A numerical estimate of the size of the chaotic zones. *Icarus* **88**, 266–291 (1990).
7. J. Laskar, "A few points on the stability of the Solar System" in *Symposium-International Astronomical Union* (Cambridge University Press, 1992), vol. 152, pp. 1–16.
8. L. J. Lourens *et al.*, Astronomical pacing of late Palaeocene to early Eocene global warming events. *Nature* **435**, 1083–1087 (2005).
9. H. Pälike *et al.*, The heartbeat of the Oligocene climate system. *Science* **314**, 1894–1898 (2006).
10. J. A. van Dam *et al.*, Long-period astronomical forcing of mammal turnover. *Nature* **443**, 687–691 (2006).
11. P. E. Olsen *et al.*, Mapping solar system chaos with the Geological Orrery. *Proc. Natl. Acad. Sci. U.S.A.* **116**, 10664–10673 (2019).
12. L. B. Clemmensen, D. V. Kent, M. Mau, O. Mateus, J. Milán, Triassic lithostratigraphy of the Jameson Land Basin (central east Greenland), with emphasis on the new Fleming Fjord Group. *Bull. Geol. Soc. Denmark* **68**, 95–132 (2020).
13. D. V. Kent, L. B. Clemmensen, Northward dispersal of dinosaurs from Gondwana to Greenland at the mid-Norian (215–212 Ma, Late Triassic) dip in atmospheric pCO<sub>2</sub>. *Proc. Natl. Acad. Sci. U.S.A.* **118**, e2020778118 (2021).
14. F. J. Jenkins *et al.*, Late Triassic continental vertebrates and depositional environments of the Fleming Fjord Formation, Jameson Land, east Greenland. *Medd. Grøn. Geosci.* **32**, 1–25 (1994).
15. M. Marzola, O. Mateus, J. Milan, L. B. Clemmensen, A review of Palaeozoic and Mesozoic tetrapods from Greenland. *Bull. Geol. Soc. Denmark* **66**, 21–46 (2018).
16. L. B. Clemmensen, Triassic rift sedimentation and palaeogeography of central East Greenland. *Bull. Grønlands geol. Unders.* **136**, 72 (1980).
17. L. B. Clemmensen, Triassic lithostratigraphy of East Greenland between Scoresby Sund and Kejser Franz Josephs Fjord. *Bull. Grønlands geol. Unders.* **139**, 56 (1980).
18. L. B. Clemmensen, D. V. Kent, F. A. Jenkins Jr., A Late Triassic lake system in East Greenland: Facies, depositional cycles and palaeoclimate. *Palaeogeogr. Palaeoclimatol. Palaeoecol.* **140**, 135–159 (1998).
19. L. B. Clemmensen *et al.*, The vertebrate-bearing Late Triassic Fleming Fjord Formation of central East Greenland revisited: Stratigraphy, palaeoclimate and new palaeontological data. *Geol. Soc. Lond. Spec. Publ.* **434**, 31–47 (2016).
20. T. Sulej *et al.*, The earliest-known mammaliaform fossil from Greenland sheds light on origin of mammals. *Proc. Natl. Acad. Sci. U.S.A.* **117**, 26861–26867 (2020).
21. D. V. Kent, L. B. Clemmensen, Paleomagnetism and cycle stratigraphy of the Triassic Fleming Fjord and Gipsdalen formations of East Greenland. *Bull. Geol. Soc. Denmark* **46**, 121–136 (1996).
22. D. V. Kent *et al.*, Empirical evidence for stability of the 405-kiloyear Jupiter-Venus eccentricity cycle over hundreds of millions of years. *Proc. Natl. Acad. Sci. U.S.A.* **115**, 6153–6158 (2018).
23. D. V. Kent, P. E. Olsen, G. Muttoni, Astrochronostratigraphic polarity time scale (APTS) for the Late Triassic and Early Jurassic from continental sediments and correlation with standard marine stages. *Earth Sci. Rev.* **166**, 153–180 (2017).
24. M. R. Talbot, K. Holm, M. A. J. Williams, "Sedimentation in low-gradient desert margin systems: A comparison of the Late Triassic of northwest Somerset (England) and the late Quaternary of east-central Australia" in *Paleoclimate and Basin Evolution of Playa Systems*, M. R. Rosen, Eds. (Geological Society of America, vol. 289, 1994).
25. M. Mau, C. J. Bjerrum, L. B. Clemmensen, Late Triassic paleowinds from lacustrine wave ripple marks in the Fleming Fjord Group, central East Greenland. *Palaeogeogr. Palaeoclimatol. Palaeoecol.* **586**, 110776 (2022).
26. P. E. Olsen, D. V. Kent, Long-period Milankovitch cycles from the Late Triassic and Early Jurassic of eastern North America and their implications for the calibration of the Early Mesozoic time-scale and the long-term behaviour of the planets. *Philos. Trans. Royal Soc. A* **357**, 1761–1786 (1999).
27. T. Vollmer *et al.*, Orbital control on Upper Triassic Playa cycles of the Steinmergel-Keuper (Norian): A new concept for ancient playa cycles. *Palaeogeogr. Palaeoclimatol. Palaeoecol.* **267**, 1–16 (2008).
28. J. Sha *et al.*, Triassic-Jurassic climate in continental high-latitude Asia was dominated by obliquity-paced variations (Junggar Basin, Ürümqi, China). *Proc. Natl. Acad. Sci. U.S.A.* **112**, 3624–3629 (2015).
29. R. C. Surdam, C. A. Wolfbauer, Green River Formation, Wyoming: A playa-lake complex. *Geol. Soc. Am. Bull.* **86**, 335–345 (1975).
30. T. K. Lowenstein, R. V. Demicco, Elevated Eocene atmospheric CO<sub>2</sub> and its subsequent decline. *Science* **313**, 1928 (2006).
31. A. G. Fischer, L. T. Roberts, Cyclicity in the Green River formation (lacustrine Eocene) of Wyoming. *J. Sediment. Res.* **61**, 1146–1154 (1991).
32. S. R. Meyers, Resolving Milankovitchian controversies: The Triassic Latemar Limestone and the Eocene Green River Formation. *Geology* **36**, 319–322 (2008).
33. G. M. Muttoni, "Magnetostratigraphy" in *Encyclopedia of Geology*, D. Alderton, S. A. Elias, Eds. (Elsevier Ltd., ed. 2, 2021), pp. 689–697.
34. M. Ikeda, R. Tada, Reconstruction of the chaotic behavior of the solar system from geologic records. *Earth Planet. Sci. Lett.* **537**, 116168 (2020).
35. L. A. Hinnov, F. J. Hilgen, "Cyclostratigraphy and astrochronology" in *Cyclostratigraphy and Astrochronology. The Geologic Time Scale 2012*, F. M. Gradstein, J. G. Ogg, M. D. Schmitz, G. M. Ogg, Eds. (Elsevier, Amsterdam, vol. 1, 2012), pp. 63–83.
36. C. Ma, S. R. Meyers, B. B. Sageman, Theory of chaotic orbital variations confirmed by Cretaceous geological evidence. *Nature* **542**, 468–470 (2017).
37. S. Manabe, K. Bryan Jr., CO<sub>2</sub>-induced change in a coupled ocean-atmosphere model and its paleoclimatic implications. *J. Geophys. Res. Oceans* **90**, 11689–11707 (1985).
38. D. F. Mantsis, A. C. Clement, A. J. Broccoli, M. P. Erb, Climate feedbacks in response to changes in obliquity. *J. Clim.* **24**, 2830–2845 (2011).
39. D. F. Mantsis *et al.*, The response of large-scale circulation to obliquity-induced changes in meridional heating gradients. *J. Clim.* **27**, 5504–5516 (2014).
40. D. J. Thomson, "Spectrum estimation and harmonic analysis" in *Proceedings of the IEEE* (IEEE, vol. 70, 1982) pp. 1055–1096.
41. M. Li, L. Hinnov, L. Kump, Acycle: Time-series analysis software for paleoclimate research and education. *Comput. Geosci.* **127**, 12–22 (2019).
42. C. Torrence, G. P. Compo, A practical guide to wavelet analysis. *Bull. Am. Meteorol. Soc.* **79**, 61–78 (1998).
43. S. R. Meyers, Astrochron: An R package for astrochronology (2014). <https://cran.r-project.org/package=astrochron>. Accessed 10 September 2019.
44. D. V. Kent, G. Muttoni, Latitudinal land-sea distributions and global surface albedo since the Cretaceous. *Palaeogeogr. Palaeoclimatol. Palaeoecol.* **585**, 110718 (2022).

## Supplementary Information for Planetary chaos and inverted climate phasing in the Late Triassic of Greenland

Malte Mau, Dennis V. Kent, Lars B. Clemmensen

To whom correspondence may be addressed: Dennis V. Kent or Lars B. Clemmensen  
Email: [dvk@ldeo.columbia.edu](mailto:dvk@ldeo.columbia.edu) or [larsc@ign.ku.dk](mailto:larsc@ign.ku.dk)

### This PDF file includes:

Supplementary text  
Figures S1 to S11  
Table S1  
SI References

### Other supplementary materials for this manuscript include the following:

SI dataset (separate Microsoft Excel file)

### Supplementary Information Text

#### 1. Geological setting

During Late Triassic times, the Jameson Land Basin was a part of a large rift system separating Greenland from Norway prior to the opening of the Atlantic (1). The Late Triassic deposits found in this basin are predominantly lacustrine and playa sediments forming the Fleming Fjord Group (2). The studied lacustrine succession comprises the Ørsted Dal Formation in the uppermost part of the Fleming Fjord Group. In the central and eastern part of the basin, the Ørsted Dal Formation is divided into the Carlsberg Fjord Member and the overlying Tait Bjerg Member, which are respectively 120 m and 50-60 m thick in the study area (Fig. S1a). The Carlsberg Fjord Member generally consists of red-brown to purple massive mudstones punctuated by centimeter-scale red or greenish grey siltstone beds with wave ripples (Fig. S2). The overlying Tait Bjerg Member consists of light grey to yellowish marlstones interbedded with variegated siliciclastic mudstones although the base of the Tait Bjerg Member is dominated by red mudstones with a few thick light grey marlstone beds. The localities “Track Mountain” (71.406746, -22.538515) and Lepidopteriselv (71.261762, -22.520303), located at the eastern margin of the basin, were logged and sampled during fieldtrips in 2012 and 2018 to examine the Tait Bjerg Member and the Carlsberg Fjord Member respectively (Fig. S1b). The localities are correlated with lithological marker beds and magnetostratigraphic linkages to construct a composite section. The first occurrence of a several decimeter thick carbonate bed is used as the primary marker bed between the two study sites.

#### 2. Climate proxies

Lacustrine sediments are generally excellent recorders of climate change (3) and have often been used to construct cyclostratigraphic records. Lakes are especially important when studying ancient sediments in the lack of preserved marine deposits. Ancient lacustrine red-beds have been studied

with a wide range of climate proxies that successfully link sediments to orbital forcing (4-7). In this study, we have chosen to produce a broad range of proxies to determine those best suited for revealing orbital cycles in the Fleming Fjord Group. Altogether, the proxies include quantifiable lithological variations, element abundances from x-ray fluorescence (XRF), color from crushed rock samples, and magnetic properties from isothermal remanent magnetization (IRM) and magnetic susceptibility (MS). These proxies are obtained in the context of two independent datasets: a detailed stratigraphic log of the lithology and rock samples collected with a fixed sampling interval.

### **2.1. Geochemical proxies**

Geochemical analysis is a common tool for revealing climate cycles. In the literature, zirconium (Zr) is often used as a grain size proxy. Zr mainly occurs in zircon minerals and is usually enriched in coarse sediment fractions due to the tendency of zircons to maintain their original morphology during weathering and transport (8). In contrast, rubidium (Rb) mainly occurs in potassium-rich minerals such as clays and is enriched in detrital clay minerals during weathering (8). Thus, the Zr to Rb ratio (Zr/Rb) provides a grain size proxy and indicates fluctuations in precipitation and runoff. Thus, if the climate becomes more humid the Zr/Rb ratio increases. Energy-dispersive X-ray spectrometry (EDX) analyses with a scanning electron microscope (SEM) of thin sections reveal that silt sized zircons are present among the siltstone beds but are rarely found in the mudstones (Fig. S3a). This corresponds well with the assumption of a positive relation between Zr and grain size. Copper (Cu) is normally not used as a climate proxy but is known to bind with organic matter (9) and has been used as a proxy for organic matter burial (10) and to record diagenetic mobilization of copper (8). Although Cu/Rb is not a typical climate proxy and has a more complex relation to climate variations than Zr/Rb, it is a particularly good proxy for cyclic variations of the climatic controlled sediments in the Jameson Land Basin. Cu/Rb is in phase with variations in Zr/Rb and lithology and is thus most likely linked to climate fluctuations. SEM analyses of thin sections reveal that copper oxides are only found in association with inter-granular carbonate and silicate cement, and are typically less than 1  $\mu\text{m}$  in diameter (Fig. S3b). This indicates that the Cu content in the lacustrine sediments originates from diagenetic precipitation. This could be early diagenesis or possibly associated with diagenetic mobilization of Cu caused by hydrothermal fluids from Cenozoic intrusions. Thus, the enrichment of Cu in the water-conducting coarse-grained sediments with a larger volume of cement could explain the relation between the diagenesis and grain size. A dendrogram plot of some selected proxies also supports Cu/Rb as a grain size proxy (Fig. S4).

### **2.2. Rock magnetic proxies**

Magnetic properties are common climatic indicators used to construct cyclostratigraphic records in Triassic lacustrine red-beds (7). Magnetic susceptibility (MS) is commonly used as a quick measurement of the composite induced magnetization for the different magnetic minerals in a sample whereas isothermal remanent magnetization (IRM) is a convenient tool for estimating the relative concentrations of magnetite and hematite although this method is not as commonly used in red-beds. Magnetite is in most cases a detrital magnetic component whereby erosional and depositional processes affect its concentration (11). Thus, measurements of magnetic mineral concentration can be tied to changes in paleoclimate and paleoenvironment. In the studied sediments in the Jameson Land Basin, IRM reveals low concentrations of magnetite and only a small variance between facies. Hematite concentrations are estimated with “hard” isothermal remanent magnetization (HIRM) measurements, which is commonly used to estimate the absolute concentration of the weakly magnetic but high coercivity hematite and goethite in rocks with respect to highly magnetic but lower coercivity magnetite and maghemite contributions (12, 13). Hematite is considered an aridity proxy (higher HIRM equals higher aridity) and has previously been used in Late Triassic sediments on the Colorado Plateau (14). Thus, HIRM is used as aridity proxy in this study (Fig. 2).

### **2.3. Color proxies**

The color variation within the Jameson Land mudstones can be very subtle and difficult to log with the naked eye. However, color analyses can provide a record of all the subtle color variations. Color analysis is a widely used method to construct climate records of lacustrine red-beds and has been

used in Late Triassic Basins across the globe (4-7). The  $L^*$  (black-white component) and  $a^*$  (red-green component) values form the CIELAB color space are commonly used. In the Jameson Land Basin, the  $L^*$  dataset is especially good for identifying 405-kyr climate peaks (Fig. S11). While the red/green color ( $a^*$ ) variation is probably linked to hematite, the lightness component ( $L^*$ ) could be tied to carbonate precipitation (Fig. S4).

### 3. Spectral analysis

The Thomson multitaper method (MTM) provides a toolbox of statistically robust estimators to test geological records for orbitally forced cycles (11). However, the method assumes a stationary geological record, which is rarely a valid assumption for most geological records because they often undergo significant changes in accumulation rate. To account for this and to track changes in accumulation rate, an evolutionary wavelet power spectrum of a geochemical grain size proxy is first analyzed (Fig. S5). The evolutionary spectrum shows some changes in accumulation rate but identifies an average 405-kyr cycle period of 16.6 m. The global spectrum of the evolutionary wavelet power spectrum reveals two long-term cycles with periods of ~33 m and ~64 m (Fig. S5). Adjusting of the long-term cycles to the average 405-kyr cycle of 16.6 m translates to periods of ~800 kyr and ~1600 kyr respectively. Tuning of the record with the 405-kyr metronome reveals periods of 853 kyr and 1707 kyr interpreted as the Mars-Earth grand cycles ( $s_4 - s_3$  and  $g_4 - g_3$ ). The veracity of the presumed  $s_4 - s_3$  signal is tested by comparing the untuned  $s_4 - s_3$  filter (33 m or ~850 kyr) with the amplitude modulation of an untuned ~40-kyr (2 m) filter (Hilbert filter). Because the  $s_4 - s_3$  signal is a modulation of the obliquity signal, the two filters should match. The filters and MTM analyses of the filters show a good match indicating that the presumed  $s_4 - s_3$  signal is in fact a modulation of the obliquity signal (Fig. S6).

MTM analyses are performed on the Jameson Land Basin Zr/Rb record and the Newark Basin depth rank record of the corresponding time interval (Fig. S7). The tuning of the Zr/Rb record is based on the 405-kyr metronome and magnetostratigraphic correlation to the N-H APTS (Fig. S10). In the Jameson Land Basin, significant (>90% CL) spectral peaks of around 1707 kyr, 853 kyr, 405 kyr, 103 kyr, 66 kyr, 42 kyr, 33 kyr, and 25 kyr are identified. In the contemporaneous interval in the Newark Basin, significant (>95% CL) spectral peaks occur at around 1725 kyr, 406 kyr, 130 kyr, 99 kyr, 78 kyr, 30 kyr, 28 kyr, and 23 kyr. The 405-kyr cycle in the Jameson Land Basin can be correlated in period even if out of phase with the 405-kyr cycle in the Newark Basin. The 99- and 130-kyr cycles in the Newark Basin corresponds to short eccentricity and can be correlated with the merged 102-kyr signal in the Jameson Land Basin. We hesitate to interpret the 25 – 66 kyr peaks in the Jameson Land Basin as precession and obliquity cycles which are likely shifted in frequency and smeared due to accumulation rate variability and low sampling resolution. The accumulation rate variability is likely a result of perturbation by numerous intraformational conglomerates and surfaces with desiccation cracks. These events indicate frequent periods with erosion or non-deposition and thus small hiatuses that create a jittered signal. In fact, models on the effect of jitter on spectral peaks show that jitter will shift the position of expected peaks to lower frequencies and smear spectral peaks, which has a significant impact on the attainable power of an orbital signal (15). The magnitude of the shift is frequency dependent meaning that high frequency cycles are affected more than low frequency cycles due to reduced relative resolution. Consequently, jitter in the form of short-term accumulation rate variability creates an apparent shift of the shorter sedimentary cycles, in this case the obliquity and precession cycles, but has a limited effect on low frequency cycles with a higher relative sample resolution. Frequency shifting and smearing of precession and obliquity periods is documented in the Late Triassic lacustrine deposits of the Newark Basin in eastern North American and the Junggar Basin in China even with much higher sediment accumulation rates (4, 16). The frequency shifts in these basins are of similar magnitude and are also interpreted as a consequence of accumulation rate variability.

Another potential contamination of the preserved astronomical signal is autogenic variability within the depositional system (17, 18). Several physical and numerical experimental studies have identified repetitive autogenic patterns in clastic deposits that can breach the 95% confidence levels in common statistical tests (18). These processes also include autogenic lake processes. For

example, Ref. 19 observed autogenic cycles of lake formation in a relay ramp system. The apparent period of these lake cycles is in the order of  $10^4$ - $10^5$  years and can thus be confused with periods of orbital cycles. Thus, there is potential for some degree of influence from autogenic processes on the Jameson Land Basin sediments. However, autogenic processes tend to have the most severe impact on shallow marine systems and fluvial systems leaving lake systems less affected (17). Furthermore, statistical tests of multiple proxies exceeding the 95% and 99% confidence levels and matching the expected periods of astronomical cycles strongly support the interpretation of a depositional system mainly influenced by allogenic forcing. Thus, the effect of autogenic processes on the lake succession in the Jameson Land Basin are probably minimal on long period variations.

#### 4. Magnetostratigraphy

The magnetostratigraphic record from samples collected at the Lepidopteriselv locality can be readily correlated to a composite magnetostratigraphic record constructed from a 1992 expedition to Tait Bjerg (20) and a 1995 expedition to “Track Mountain” (21) (Fig. S8). Aside from a relatively minor and easily removed overprint acquired along the present-day field, the most ubiquitous component of the Lepidopteriselv section is a strong normal polarity B component (Fig. S9) with the same direction as found in many of the samples from other sections of the Fleming Fjord Group in the Jameson Land Basin. The B component is ascribed (20) to thermochemical overprinting associated with the early Cenozoic North Atlantic igneous province. Nonetheless, a dual polarity high unblocking temperature characteristic magnetization can be isolated in the majority of the samples analyzed to construct a magnetostratigraphy. Four magnetozones are delineated and readily correlated to magnetozones F2r, F3n, F3r and F4n from the Carlsberg Fjord Member in the “Track Mountain” -Tait Berg composite section (21) (Fig. S10). The main difference is that the correlative complete magnetozones (F3n and F3r) are about 27% thicker in the Lepidopteriselv section (60 m for F3n+r compared to 47.4 m in the “Track Mountain”-Tait Berg composite section), implying a correspondingly higher sediment accumulation rate at Lepidopteriselv over at least this interval. Reassuringly, the Carlsberg Fjord Member as mapped is also proportionately thicker: 123 m in Lepidopteriselv compared to 95 m in the “Track Mountain” -Tait Berg composite section which corresponds to a ~30% thickness difference. Another difference between the records is the thin normal polarity interval F3n.1r which is not found in the Lepidopteriselv section where it is probably missing due to low sampling rate or thermochemical overprinting. The rock samples and log used to describe the Tait Bjerg Member in this study is acquired at the same locality as the 1995 magnetostratigraphic record. Thus, we use the top part of the “Track Mountain” -Tait Berg composite section to expand the polarity record used in this study. This expansion includes the rest of magnetozone F4n and F4r although only a few data points are available in the topmost part of this interval so that the boundaries between F4r, F4n and F5n are not well defined. In accordance with the most likely magnetostratigraphic age model identified in a previous study (21), polarity zones F2r to F5n are correlated with polarity chrons E14r to E17n in the Newark Basin APTS (Fig. S10), which provides a mean accumulation rate of 35.4 m/Myr for the interval 40-160 m.

Data table with characteristic (C component) magnetization directions and VGP latitudes provided (Tab. S1).

#### 5. Orbital and magnetostratigraphic tuning

The most desirable way to find the duration of orbitally paced cycles is to tune the spectrum to theoretical variations in insolation for eccentricity, obliquity and precession (11). However, cyclostratigraphic records from remote geological ages (>50 Ma) cannot be calibrated to present complete astronomical solutions due to large uncertainties and chaotic behavior (22). Another powerful way to test if a record is orbitally paced is to establish an age model based on age controls such as biostratigraphy or magnetostratigraphy and then use the 405-kyr long eccentricity cycle as a chronometer. The use of this method relies on the prominent amplitude and stability of the 405-kyr cycle, which originates from the gravitational interaction with Jupiter and Venus. Due to the large mass of Jupiter, the 405-kyr cycle period should be highly stable as far back as at least 250 Ma (23), which has been verified empirically (24). Thus, the 405-kyr cycle is a prominent metronome in many deep-time cyclostratigraphic records (22, 25).

In the Jameson Land Basin, an initial age model is based on magnetostratigraphic correlation with the Newark Basin, which is calibrated with the 405-kyr metronome. To construct a floating age model of the Ørsted Dal Formation, individual 405-kyr peaks are picked out with a Gaussian-weighted moving average filters and bandpass filters of multiple climate proxies (Fig. S11). Ten full 405-kyr cycles are identified and each named after the stratigraphic unit they are found in followed by a number starting with one at the base of each unit. This gives a total time span of about 4.3 Myr. The Carlsberg Fjord Member spans eight 405-kyr cycles corresponding to 3.24 Myr and the lower part of the Tait Bjerg Member spans about two cycles corresponding to 810 kyr. The floating age model is anchored by the magnetostratigraphy, which is linked via the APTS to high precision U-Pb dated levels, by assuming that the peak between 405-kyr cycles CBF-2 and CBF-3 corresponds to the boundary between magnetozone E14 and E15 from the Newark Basin. Magnetozone ages from the Newark Basin and the filtered 405-kyr peaks and valleys are used for tuning of the depth record. The final age model gives the studied succession an age of 214.36 - 210.01 Ma, which is in the mid-late Norian (23).

The accumulation rate is calculated from the 405-kyr filter using the stratigraphic positions of filter peaks. The accumulation rate varies from 25.6 m/Myr to 48.4 m/Myr with a mean rate of 37.6 m/Myr (Fig. S11). This fits very well with the 35.4 m/Myr mean accumulation rate calculated with magnetostratigraphic correlation via other Jameson Land Basin sections (Fig. S10). Alternative age models (21) would correspond to mean accumulation rates of 78.1 m/Myr and 62.9 m/Myr, which cannot be accommodated by the cyclostratigraphic interpretation from this study. Furthermore, the alternative age models are not very likely as they would require either a low magnetostratigraphic fidelity or large abrupt changes in sediment accumulation rate (21). In conclusion, the magnetostratigraphy and cyclostratigraphy are mutually supportive in our interpretation of the sedimentary cyclicity and chronostratigraphy.

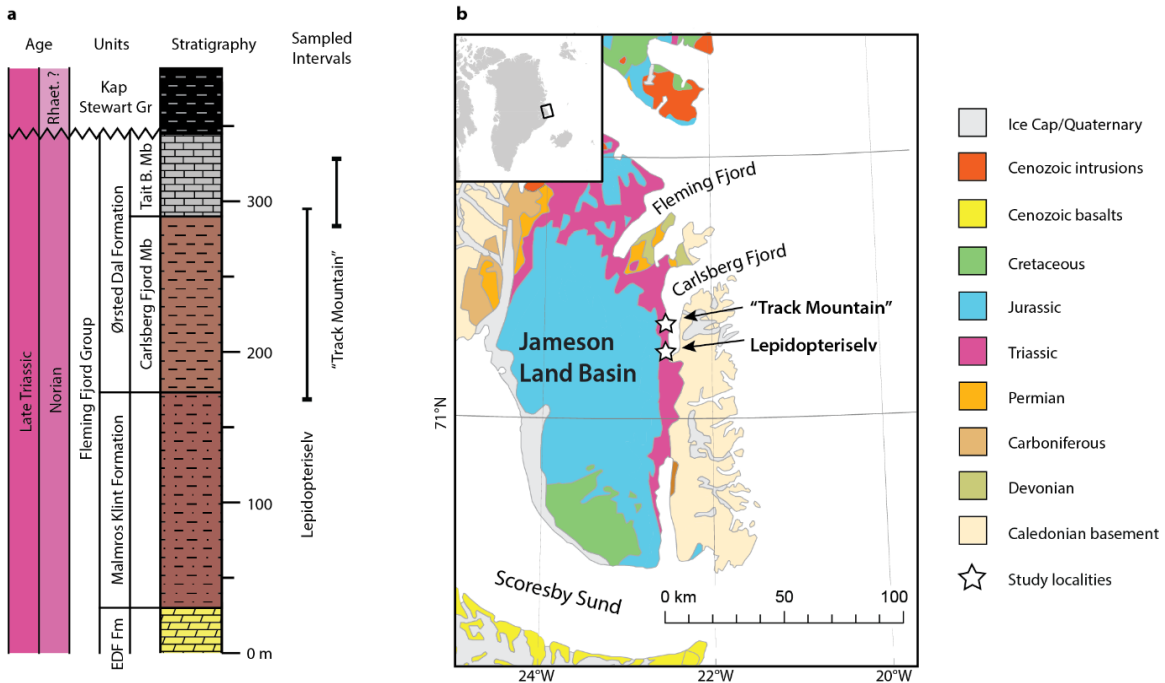


**Fig. S1.** Geological setting of the studied lake succession. **(a)** Simplified stratigraphic log at the Lepidopteriselv study site. The sampled intervals of the two study localities are marked with a black line. **(b)** Geological map of Jameson Land with the Lepidopteriselv (71.261762, -22.520303) and "Track Mountain" (71.406746, -22.538515) study localities indicated by stars. Modified from Ref. 27.

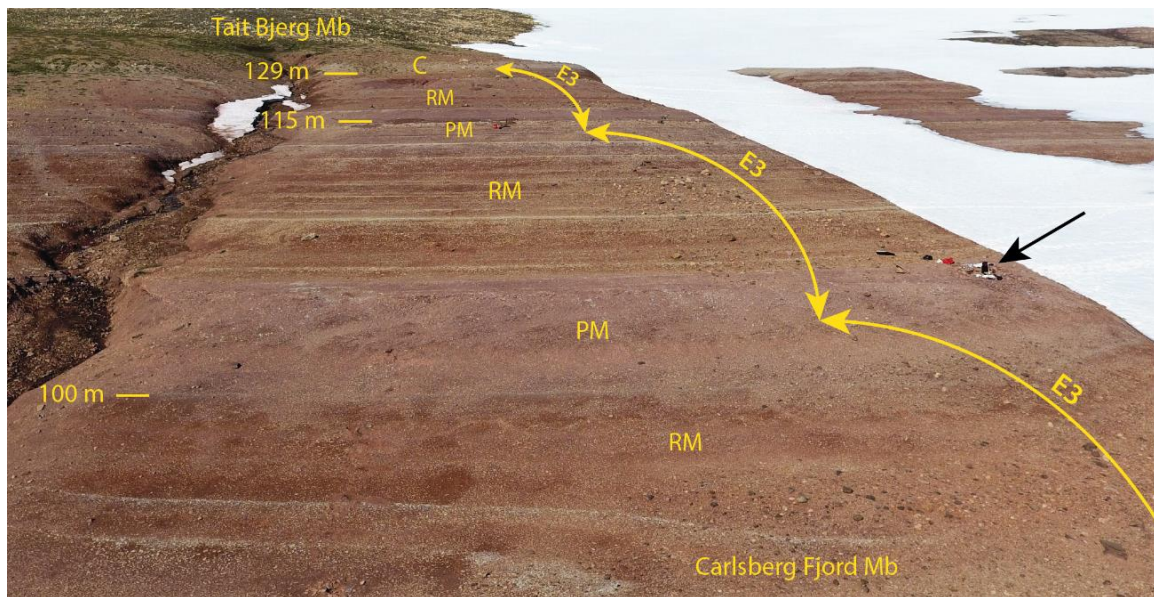


**Fig. S2.** Drone photo of the upper part of the Carlsberg Fjord Member at the Lepidopteriselv study site. Cyclic bedding is expressed as alternating red (RM) and purple (PM) mudstones, and bundled grey to red thin siltstone beds. The long eccentricity cycle (E3) is clearly visible as color variation with increased precipitation and run-off occurring in the coarse-grained purple mudstone intervals. A several meter thick grey carbonate bed is marking the boundary between the Carlsberg Fjord Member and the Tait Bjerg Member. Meter marks correspond to the stratigraphic level of the studied succession. For scale, a paleontologist working in a quarry is marked with a black arrow.

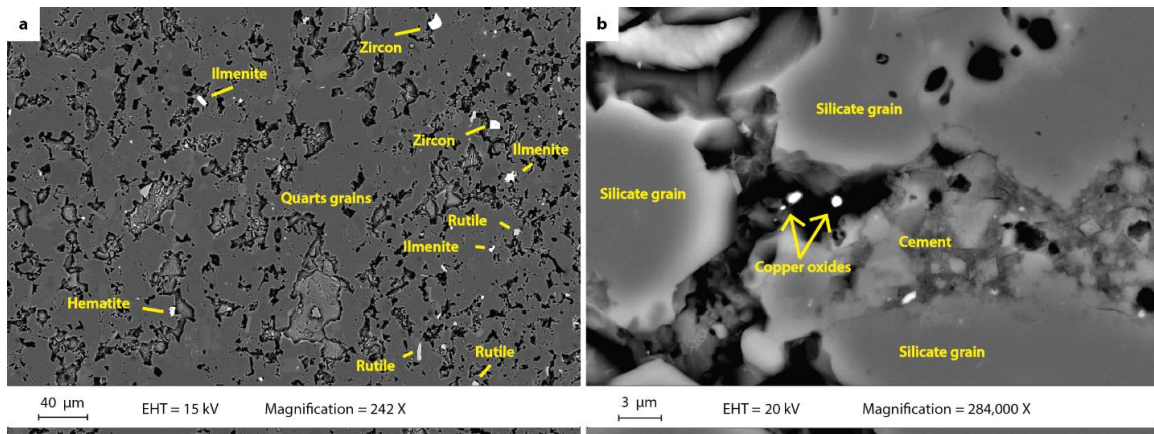


**Fig. S3.** SEM micrographs of a siltstone from the Carlsberg Fjord Member. Minerals are identified with energy-dispersive X-ray spectrometry. **(a)** Micrograph showing quartz grains and some more dense minerals shown as white objects. Zircon is commonly found in the siltstones while they are rarely found in the mudstones. **(b)** Micrograph showing micrometer scale copper oxides sitting in the inter-granular cement.

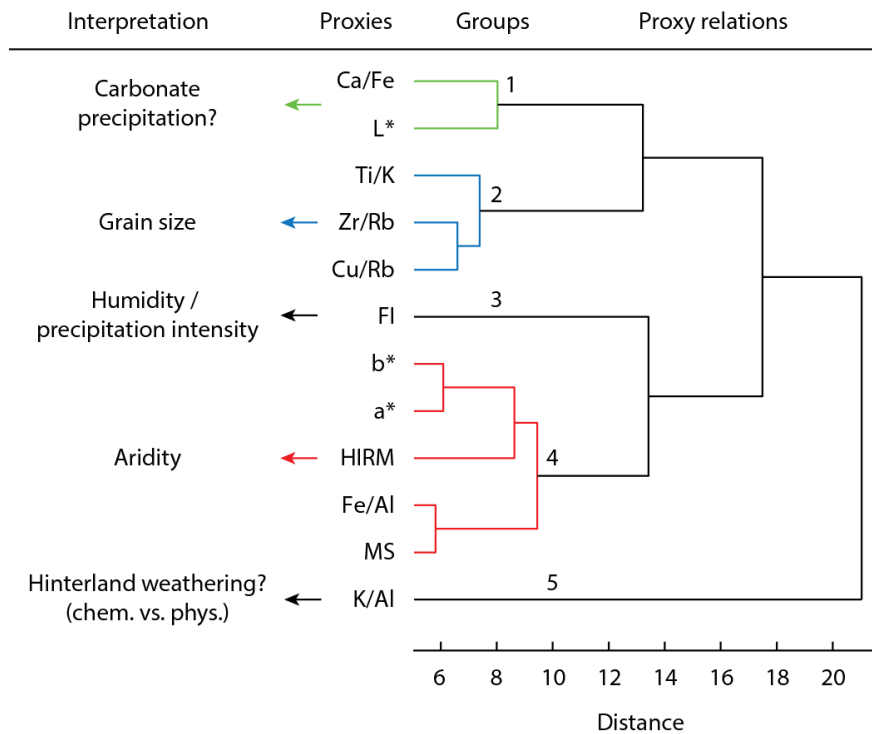


**Fig. S4.** Dendrogram (hierarchical cluster tree) computed with the inner squared distance (ward) algorithm in Matlab. The dendrogram shows which proxies are alike by calculating linkage distances between clusters. The proxies are grouped into five groups based to the best matching MTM spectra (cut off distance = 10). We suggest that group one could be linked to carbonate precipitation. Group two is interpreted as grain size proxies. Group three is humidity/precipitation intensity proxy. Group four is aridity proxies linked to hematite. Group five could be a hinterland weathering proxy (7). The dendrogram is based on MTM spectra of the 0-60 m interval in the studied succession following the method of Ref. 28. L\*: black-white color component, a\*: red-green color component, b\*: blue-yellow color component, FI: flooding index, HIRM: hard isothermal remanent magnetization, MS: magnetic susceptibility.



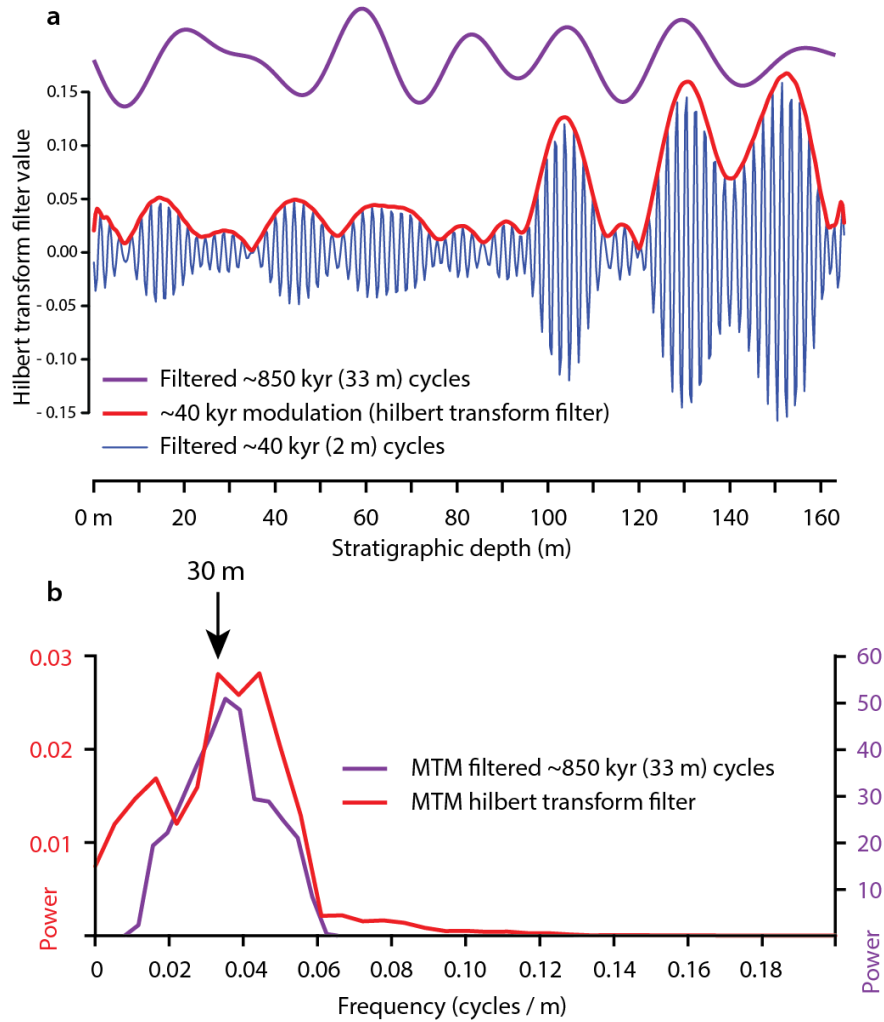


**Fig. S6.** Filtered ~850-kyr cycles compared with modulation of the filtered ~40 kyr cycles indicates that the ~40-kyr obliquity cycle is modulated by the ~850-kyr cycle. (a) Purple filter: Bandpass filtered (frequency range: 0.023 to 0.05 cycles/m) ~850-kyr (33 m) cycle based on the un-tuned flooding index. Blue filter: Bandpass filtered (frequency range: 0.48 to 0.53 cycles/m) ~40-kyr (2 m) cycle based on the un-tuned clipped Cu/Rb record. Red filter: Hilbert transform filter of the filtered ~40-kyr cycle. This filter shows the amplitude modulation of the ~40-kyr filter. (b) MTM spectra of the filtered ~850-kyr cycles (purple) and ~40-kyr cycles (red). The spectra show a common peak around the 30-m mark corresponding to ~850 kyr.

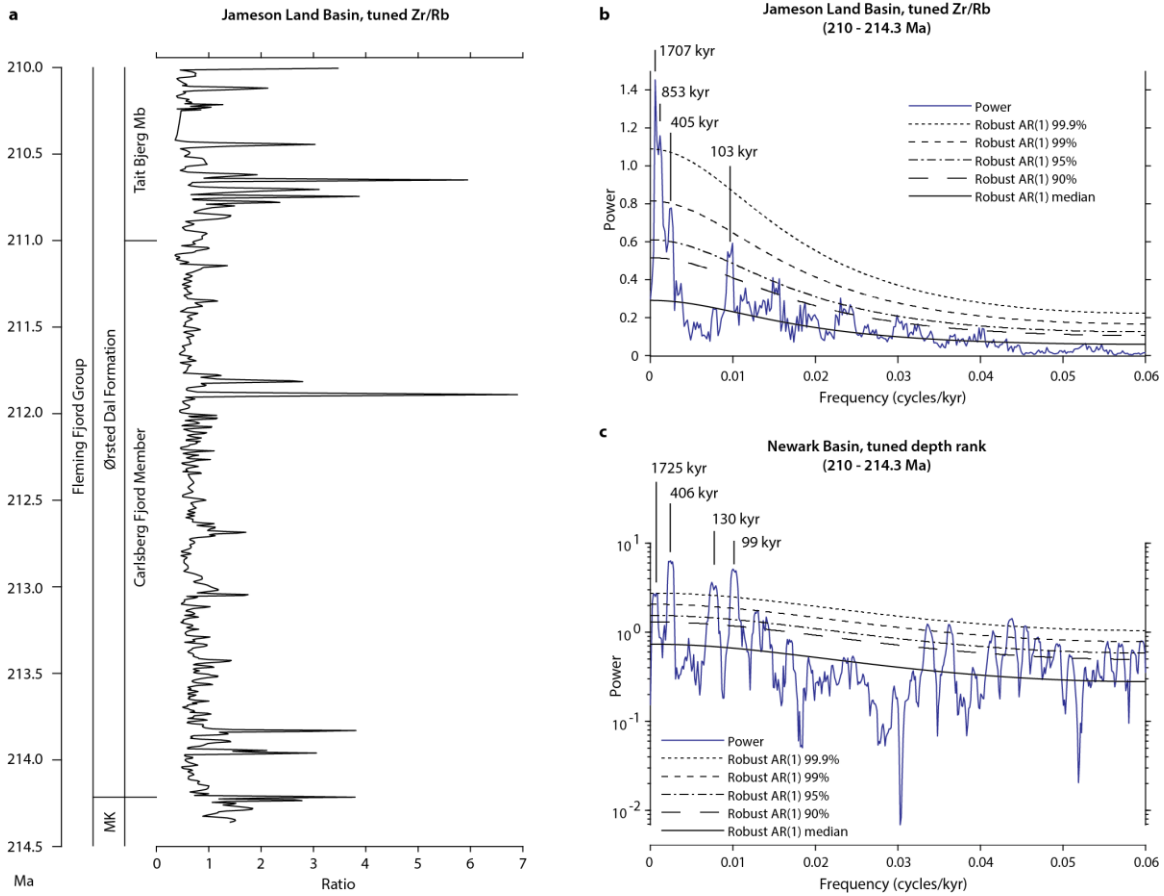


**Fig. S7.** Comparison of statistical analyses (Thompson multitaper method analyses) of the Jameson Land Basin and the Newark Basin. **(a)** Zr/Rb record tuned to magnetochrons and the 405-kyr metronome. **(b)** MTM spectrum based on the tuned Zr/Rb record from the Jameson Land Basin (Fig. S7a). Spectral peaks we consider important are the 1707, 405 and 103-kyr eccentricity cycles and the 853-kyr inclination modulation of obliquity; less well-resolved shorter period peaks are presumably related to obliquity and precession cycles. **(c)** Contemporaneous MTM spectrum of the Newark Basin depth rank index showing 1725, 405 and split 130 and 99 kyr eccentricity cycles complementary to those in the Jameson Land MTM spectrum but with no orbital inclination peak of ~850-kyr; poorly resolved shorter period peaks are also present.

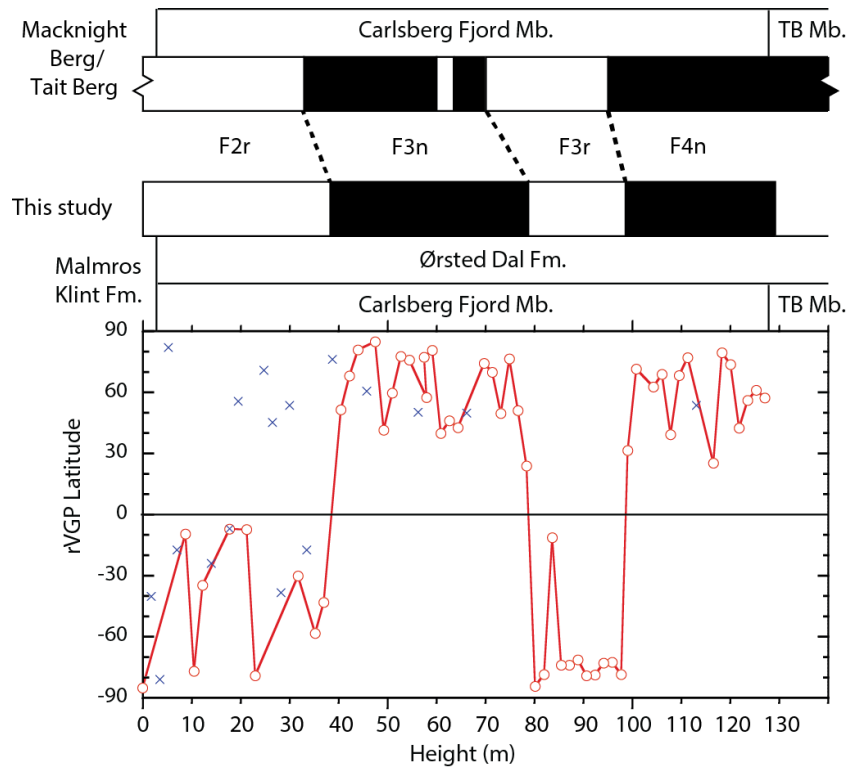


**Fig. S8.** Correlation between the magnetostratigraphic record from this study and another record from the Jameson Land Basin (21). The four magnetozones from this study correlate well with magnetozones F2r, F3n, F3r, and F4n from the Macknight Berg -Tait Berg composite section. Although, there seems to be an offset between boundaries. Magnetic measurements shown with red circles and blue crosses. rVGP latitude is the rotated latitude of the calculated virtual geomagnetic pole for the sample site ChRM compared to the mean overall paleomagnetic pole; rVGP latitudes approaching +90° and -90° signify normal, n, and reverse, r, polarity. The blue crosses mark samples that did not provide acceptable paleomagnetic data.

# Lepidoteriselv Section, Fleming Fjord Group, Jameson Land basin

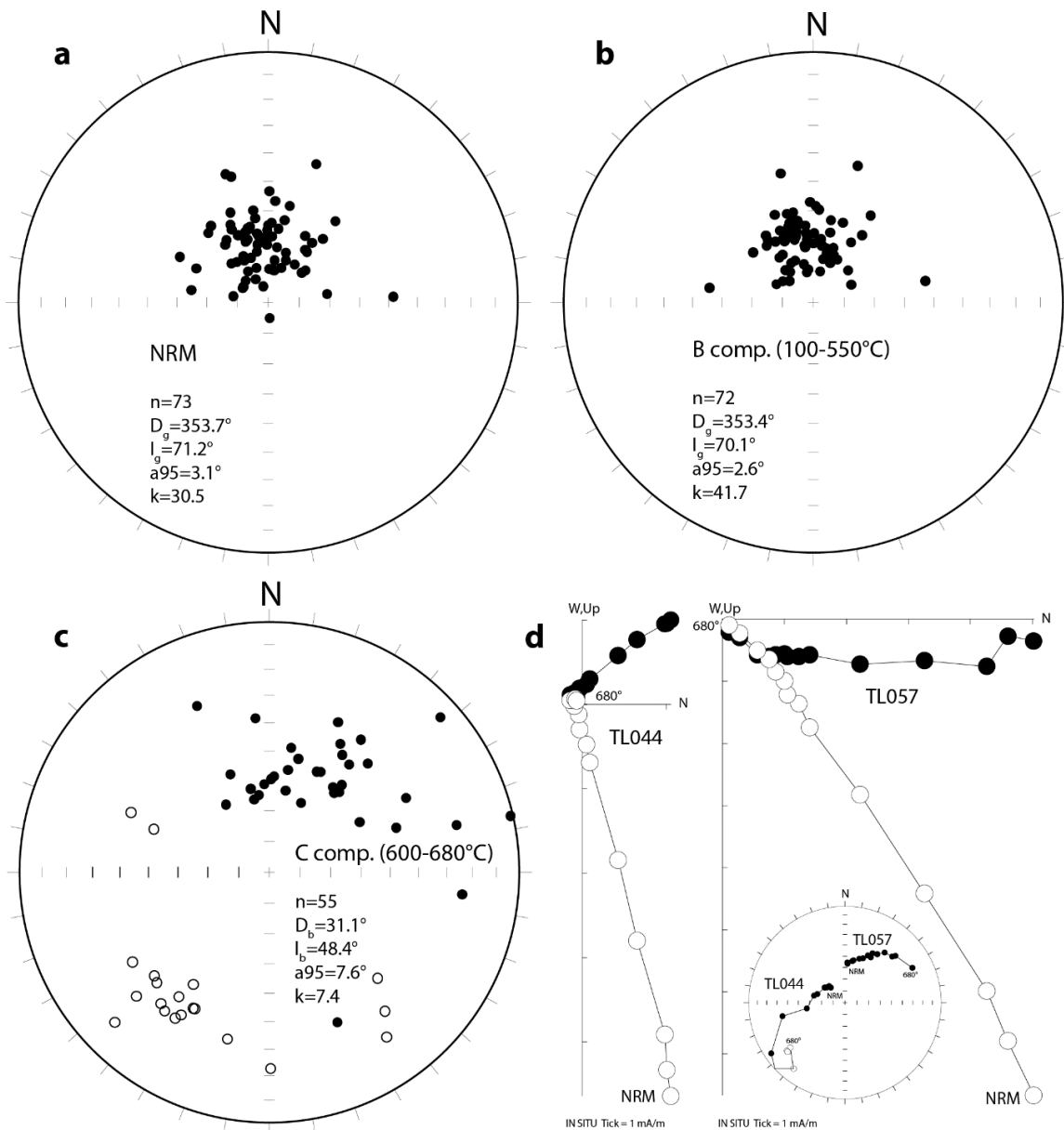


**Fig. S9.** Thermal demagnetization data on samples from Lepidoteriselv section of Fleming Fjord Group. **(a)** Natural remanent magnetization (NRM) directions of samples collected from the section. **(b)** B component magnetizations directions isolated in all 72 samples by thermal demagnetization as calculated by principal component analysis in 7 temperature steps between 100° and 550°C with MAD angles typically 5° or less. **(c)** Characteristic or C component magnetization directions isolated by thermal demagnetization as calculated by principal component analysis in 2 to 5 temperature steps between 600° and 680°C with MAD angles 20° or less. **(d)** Examples of thermal demagnetization data shown as vector end point diagrams; both samples have a predominant B component magnetization (north and down) overprinting either a reverse (TL044) or normal (TL057) polarity C component interpreted as the characteristic magnetization used for the magnetostratigraphy. Thermal demagnetization steps were done at 100, 200, 300, 400, 500, 525, 550, 575, 600, 625, 650, 675, and 680°C.

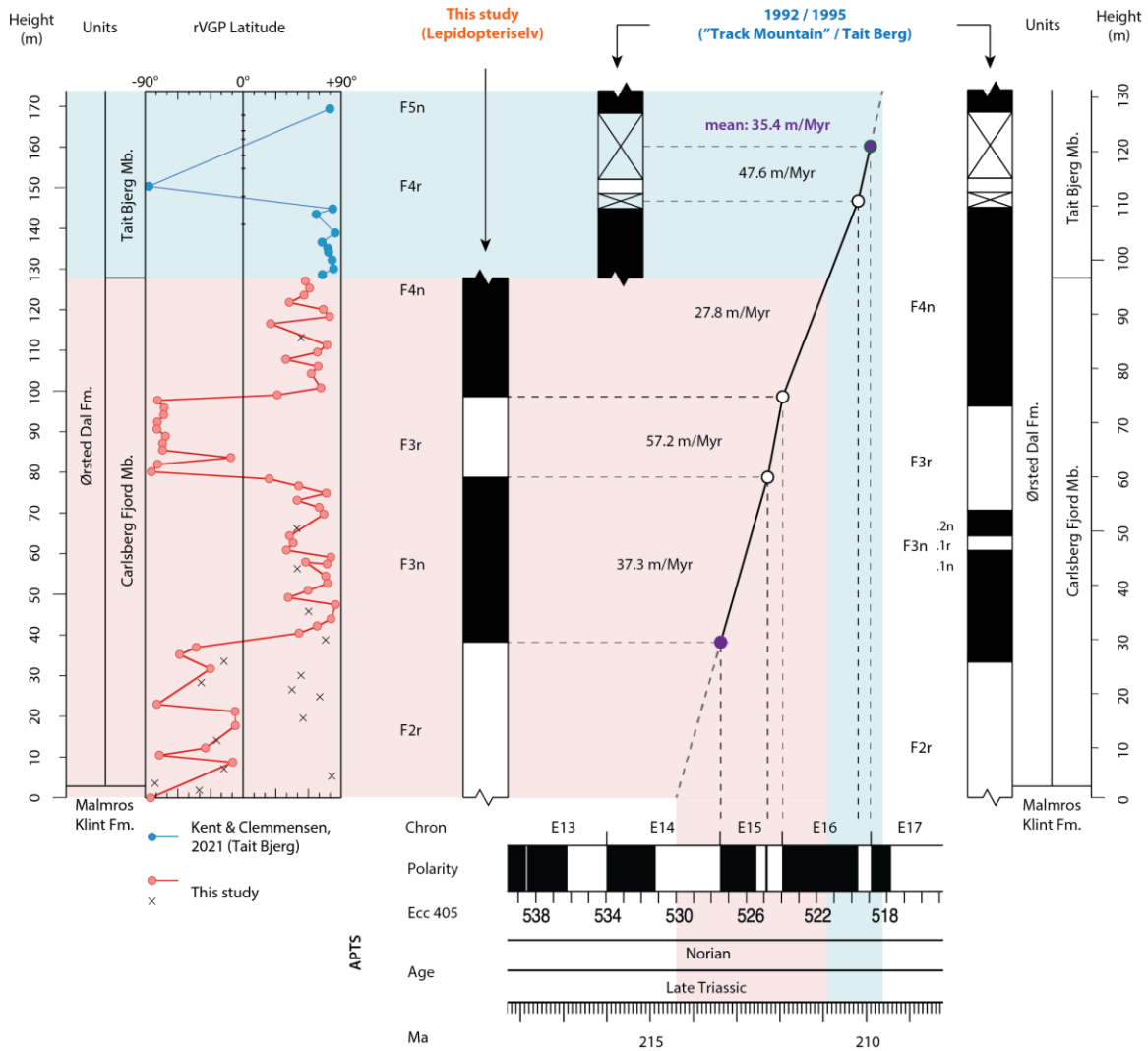


**Fig. S10.** Correlation of the polarity record from this study with the Astro-chronostratigraphic polarity time scale (26) and a polarity record from a previous magnetostratigraphic study from the “Track Mountain”/Taitbjerg locations in the Jameson Land Basin (21). The four magnetozones from this study correlate well with magnetozones F2r, F3n, F3r, and F4n from the 1992/1995 “Track Mountain”-Tait Berg composite section. Accumulation rates are calculated by correlating with the APTS in accordance with Ref. 21 model A. This gives a mean accumulation rate of 35.4 m/Myr. Crossed areas in the polarity record mark intervals with poor data points. Magnetic measurements from the Lepidopteriselv site are shown with red circles (accepted data) and black crosses (discarded data) while the blue circles represent measurements from the “Track Mountain”-Tait Berg section. Thus, the black crosses mark samples that did not provide acceptable paleomagnetic data. rVGP latitude is the rotated latitude of the calculated virtual geomagnetic pole for the sample site ChRM compared to the mean overall paleomagnetic pole; rVGP latitudes approaching +90° and -90° signify normal, n, and reverse, r, polarity.



**Fig. S11.** The long eccentricity (405 kyr) cycle is used as a chronometer to construct a floating age model, which is anchored with magnetostratigraphy. This gives the studied lake succession a time span of 210 to 214.3 Ma. Control points from 405-kyr peaks and valleys and polarity chron boundaries are used to tune the polarity record and climate proxies. Control points from the 405-kyr peaks and polarity chron boundaries are shown in the figure. The 405-kyr cycle is filtered from the lightness color record, the Zr/Rb record and the Cu/Rb record and each cycle peak is traced across the figure with dashed lines. The 405-kyr peaks are also seen in flooding index record. Red filters: Gaussian-weighted moving average filter with window length of 35 m. Orange filters: Bandpass filter with a frequency range of 0.4 to 1.0 cycles/m. The accumulation rate is based on the 405-kyr filter peaks and have a mean value of 37.6 m/Myr marked with a red dashed line.

**Table S1.** Characteristic (C component) magnetization directions and VGP latitudes for samples collected in 2018 field sampling season from Carlsberg Fjord and Tait Berg members of Ørsted Dal Formation of Fleming Fjord Group in Lepidopteriselv locality. ID is sample identification (except MK/OD for contact of Malmros Klint and Ørsted Dal formations and CF/TF for contact of Carlsberg Fjord and Tait Berg members). Height is stratigraphic level above base of local section in meters, n is the number of demagnetization temperature levels from T1 to T2 (in °C) included for PCA analysis to isolate the characteristic (C component) magnetization and MAD is the maximum angular deviation of the fit anchored to the origin (29). bDec and blnc are the declination and inclination in bedding coordinates of C component and VGP bLon and VGP bLat are coordinates for corresponding virtual geomagnetic pole. rVGP lat is the latitude of the C component VGP with respect to the overall mean pole for interpreting magnetic polarity stratigraphy, positive values for normal and negative values for reverse polarity; rVGP lat values outlined in red were considered unreliable due to high MAD angles (>20°) except for sample TL67, which is interpreted as misoriented.

|    | ID    | Height, m | n | MAD  | bDec  | blnc  | VGP bLon | VGP bLat | rVGP lat | T1  | T2  |
|----|-------|-----------|---|------|-------|-------|----------|----------|----------|-----|-----|
| 0  |       |           |   |      |       |       |          |          |          |     |     |
| 1  | TL67  | 128.85    | 5 | 12.0 | 66.0  | -72.9 | 112.3    | -47.6    | 4.0      | 600 | 680 |
| 2  | CF/TB | 128.05    |   |      |       |       |          |          |          |     |     |
| 3  | TL66  | 127.10    | 5 | 5.6  | 10.0  | 48.2  | 144.5    | 47.6     | 57.2     | 600 | 680 |
| 4  | TL65  | 125.35    | 5 | 4.9  | 14.4  | 51.4  | 138.3    | 50.0     | 61.0     | 600 | 680 |
| 5  | TL64  | 123.60    | 5 | 4.4  | 11.3  | 62.8  | 139.8    | 62.4     | 56.1     | 600 | 680 |
| 6  | TL63  | 121.85    | 5 | 5.7  | 354.8 | 38.3  | 163.8    | 40.2     | 42.4     | 600 | 680 |
| 7  | TL62  | 120.10    | 5 | 6.9  | 29.0  | 41.1  | 122.3    | 39.5     | 73.5     | 600 | 680 |
| 8  | TL61  | 118.35    | 5 | 5.6  | 41.1  | 55.0  | 103.9    | 48.4     | 79.4     | 600 | 680 |
| 9  | TL60  | 116.60    | 5 | 5.3  | 327.3 | 63.8  | 206.4    | 59.8     | 25.3     | 600 | 680 |
| 10 | TL58  | 113.10    | 5 | 23.3 | 7.3   | 62.0  | 146.2    | 61.7     | 53.6     | 600 | 680 |
| 11 | TL57  | 111.35    | 5 | 6.0  | 34.7  | 35.9  | 116.8    | 34.8     | 77.1     | 600 | 680 |
| 12 | TL56  | 109.60    | 5 | 8.9  | 24.7  | 34.5  | 128.4    | 35.7     | 68.2     | 600 | 680 |
| 13 | TL55  | 107.85    | 5 | 8.5  | 347.4 | 62.1  | 176.8    | 61.4     | 39.3     | 600 | 680 |
| 14 | TL54  | 106.10    | 5 | 8.1  | 70.7  | 45.3  | 76.5     | 31.5     | 68.8     | 600 | 680 |
| 15 | TL53  | 104.35    | 5 | 3.9  | 24.7  | 65.1  | 118.4    | 63.2     | 62.6     | 600 | 680 |
| 16 | TL51  | 100.85    | 5 | 1.5  | 27.1  | 52.9  | 121.6    | 49.5     | 71.3     | 600 | 680 |
| 17 | TL50  | 99.10     | 5 | 5.6  | 338.3 | 55.4  | 187.2    | 52.9     | 31.5     | 600 | 680 |
| 18 | TL49  | 97.70     | 5 | 5.4  | 236.8 | -34.9 | 273.4    | -28.6    | -78.6    | 600 | 680 |
| 19 | TL48  | 95.95     | 5 | 11.9 | 208.7 | -37.9 | 303.2    | -37.3    | -72.6    | 600 | 680 |
| 20 | TL47  | 94.20     | 4 | 9.3  | 209.3 | -37.8 | 302.6    | -37.1    | -73.1    | 625 | 680 |
| 21 | TL46  | 92.45     | 5 | 5.1  | 227.1 | -28.2 | 284.8    | -27.2    | -78.8    | 600 | 680 |
| 22 | TL45  | 90.70     | 4 | 10.7 | 216.1 | -38.5 | 294.7    | -36.2    | -79.1    | 625 | 680 |
| 23 | TL44  | 88.95     | 5 | 14.6 | 225.9 | -15.0 | 288.1    | -20.3    | -71.4    | 600 | 680 |
| 24 | TL43  | 87.20     | 5 | 20.7 | 211.8 | -33.4 | 300.5    | -33.8    | -73.9    | 600 | 680 |
| 25 | TL42  | 85.45     | 2 | 18.7 | 212.9 | -31.3 | 299.6    | -32.2    | -74.0    | 650 | 680 |
| 26 | TL41  | 83.70     | 2 | 5.4  | 144.5 | -20.3 | 16.7     | -25.4    | -11.3    | 650 | 680 |
| 27 | TL40  | 81.95     | 5 | 20.9 | 214.2 | -45.0 | 295.4    | -41.4    | -78.5    | 600 | 680 |
| 28 | TL39  | 80.20     | 2 | 19.9 | 225.6 | -37.1 | 284.6    | -33.0    | -84.4    | 625 | 650 |
| 29 | TL38  | 78.45     | 4 | 17.2 | 336.4 | 28.4  | 184.6    | 32.1     | 23.8     | 625 | 680 |
| 30 | TL37  | 76.70     | 5 | 19.4 | 2.9   | 58.6  | 153.2    | 58.0     | 51.1     | 600 | 680 |
| 31 | TL36  | 74.95     | 5 | 20.0 | 31.9  | 44.1  | 118.3    | 41.2     | 76.4     | 600 | 680 |
| 32 | TL35  | 73.20     | 5 | 15.4 | 1.0   | 59.5  | 156.0    | 59.1     | 49.5     | 600 | 680 |
| 33 | TL34  | 71.45     | 6 | 8.2  | 25.3  | 53.4  | 123.7    | 50.3     | 69.7     | 600 | 680 |
| 34 | TL33  | 69.70     | 5 | 14.4 | 61.0  | 56.0  | 81.7     | 43.6     | 74.2     | 600 | 680 |
| 35 | TL31  | 66.20     | 5 | 25.4 | 1.1   | 51.2  | 156.0    | 50.6     | 49.8     | 600 | 680 |
| 36 | TL30  | 64.45     | 5 | 11.9 | 352.3 | 64.6  | 170.1    | 64.9     | 42.6     | 600 | 680 |
| 37 | TL29  | 62.70     | 5 | 13.1 | 356.7 | 61.2  | 162.5    | 61.0     | 46.1     | 600 | 680 |
| 38 | TL28  | 60.95     | 5 | 15.5 | 348.2 | 65.8  | 177.2    | 66.1     | 39.7     | 600 | 680 |
| 39 | TL27  | 59.20     | 5 | 16.3 | 39.8  | 52.6  | 106.4    | 46.5     | 80.6     | 600 | 680 |
| 40 | TL26  | 57.45     | 5 | 4.9  | 36.9  | 55.1  | 108.8    | 49.5     | 77.2     | 600 | 680 |
| 41 | TL25  | 58.00     | 5 | 16.6 | 10.4  | 55.9  | 142.9    | 54.8     | 57.3     | 600 | 680 |
| 42 | TL24  | 56.25     | 5 | 22.0 | 18.1  | 74.5  | 113.4    | 77.5     | 50.1     | 600 | 680 |
| 43 | TL23  | 54.50     | 5 | 11.9 | 61.5  | 37.8  | 87.9     | 29.0     | 75.8     | 600 | 680 |

|    | ID    | Height, m | n | MAD  | bDec  | bInc  | VGP bLon | VGP bLat | rVGP lat | T1  | T2  |
|----|-------|-----------|---|------|-------|-------|----------|----------|----------|-----|-----|
| 44 | TL22  | 52.75     | 5 | 10.0 | 39.3  | 56.3  | 105.3    | 50.1     | 77.5     | 600 | 680 |
| 45 | TL21  | 51.00     | 4 | 18.8 | 75.9  | 23.8  | 76.8     | 16.3     | 59.6     | 625 | 680 |
| 46 | TL20  | 49.25     | 5 | 18.9 | 96.5  | 23.4  | 57.4     | 9.5      | 41.5     | 600 | 680 |
| 47 | TL19  | 47.50     | 5 | 10.7 | 42.2  | 41.1  | 107.4    | 36.6     | 84.9     | 600 | 680 |
| 48 | TL18  | 45.75     | 5 | 33.5 | 64.5  | 4.2   | 91.2     | 10.0     | 60.6     | 600 | 680 |
| 49 | TL17  | 44.00     | 5 | 6.5  | 36.6  | 45.5  | 112.5    | 41.2     | 80.7     | 600 | 680 |
| 50 | TL16  | 42.25     | 5 | 13.6 | 47.9  | 8.6   | 106.9    | 16.6     | 68.1     | 600 | 680 |
| 51 | TL15  | 40.50     | 4 | 19.6 | 76.9  | 1.1   | 79.7     | 4.7      | 51.5     | 625 | 680 |
| 52 | TL14  | 38.75     | 5 | 46.5 | 48.8  | 23.9  | 103.8    | 24.3     | 76.2     | 600 | 680 |
| 53 | TL13  | 37.00     | 5 | 12.8 | 179.6 | -22.7 | 337.9    | -30.6    | -43.2    | 600 | 680 |
| 54 | TL12  | 35.25     | 2 | 15.1 | 194.1 | -31.9 | 320.9    | -35.4    | -58.3    | 650 | 675 |
| 55 | TL11  | 33.50     | 5 | 28.8 | 163.8 | 24.1  | 353.4    | -5.4     | -17.4    | 600 | 680 |
| 56 | TL10  | 31.75     | 5 | 9.7  | 293.3 | -39.6 | 218.6    | -14.2    | -30.1    | 600 | 680 |
| 57 | TL9   | 30.00     | 7 | 29.0 | 9.4   | 30.1  | 146.5    | 34.6     | 53.7     | 600 | 680 |
| 58 | TL8   | 28.25     | 5 | 39.0 | 287.2 | -55.1 | 219.4    | -28.3    | -38.3    | 600 | 680 |
| 59 | TL7   | 26.50     | 6 | 36.4 | 360.0 | 29.6  | 157.5    | 34.6     | 45.2     | 600 | 680 |
| 60 | TL6   | 24.75     | 5 | 40.1 | 60.6  | 22.6  | 92.0     | 20.3     | 70.7     | 600 | 680 |
| 61 | TL5   | 23.00     | 4 | 15.3 | 219.6 | -32.5 | 292.0    | -31.6    | -79.1    | 625 | 680 |
| 62 | TL4   | 21.25     | 3 | 18.7 | 134.3 | -39.3 | 31.0     | -34.5    | -7.4     | 650 | 680 |
| 63 | TL3   | 19.50     | 5 | 37.6 | 8.0   | 50.7  | 146.8    | 49.9     | 55.6     | 600 | 680 |
| 64 | TL1   | 17.75     | 5 | 38.6 | 318.8 | -35.5 | 196.0    | -5.2     | -7.0     | 600 | 680 |
| 65 | TL2   | 17.75     | 5 | 14.3 | 155.5 | 34.6  | 0.6      | 1.9      | -7.2     | 600 | 680 |
| 66 | TL76  | 14.00     | 5 | 37.2 | 157.8 | -23.9 | 2.6      | -29.7    | -24.0    | 600 | 680 |
| 67 | TL75  | 12.25     | 5 | 16.2 | 290.4 | -49.2 | 218.6    | -22.2    | -34.7    | 600 | 680 |
| 68 | TL74  | 10.50     | 5 | 17.8 | 217.1 | -31.2 | 295.0    | -31.3    | -76.9    | 600 | 680 |
| 69 | TL73  | 8.75      | 3 | 14.9 | 140.2 | -28.6 | 22.5     | -29.2    | -9.5     | 575 | 625 |
| 70 | TL72  | 7.00      | 5 | 39.2 | 261.3 | 58.4  | 269.7    | 34.0     | -17.3    | 600 | 680 |
| 71 | TL71  | 5.25      | 5 | 28.9 | 39.9  | 50.4  | 107.2    | 44.5     | 82.0     | 600 | 680 |
| 72 | TL70  | 3.50      | 5 | 30.7 | 221.0 | -53.0 | 284.9    | -46.5    | -81.0    | 600 | 680 |
| 73 | MK/OD | 3.20      |   |      |       |       |          |          |          |     |     |
| 74 | TL69  | 1.75      | 5 | 46.2 | 197.4 | 27.6  | 320.6    | -3.3     | -40.1    | 600 | 680 |
| 75 | TL68  | 0.00      | 5 | 9.9  | 228.1 | -38.1 | 281.7    | -33.1    | -85.1    | 600 | 680 |

**Dataset S1 (separate file).** Microsoft Excel file containing data on untuned Cu, Rb, Zr, Lightness, HIRM, siltstone beds and flooding index. Age model control points. Tuned Zr/Rb, flooding index and siltstone beds.

## SI References

1. Clemmensen, L. B., Kent, D. V., & Jenkins Jr, F. A. A Late Triassic lake system in East Greenland: facies, depositional cycles and palaeoclimate. *Palaeogeogr. Palaeoclimatol. Palaeoecol.* **140(1-4)**, 135-159 (1998).
2. Clemmensen, L.B., Kent, D.V., Mau, M., Mateus, O & Milán, J. Triassic lithostratigraphy of the Jameson Land Basin (central east Greenland), with emphasis on the new Fleming Fjord Group. *Bull. Geol. Soc. Denmark* **68**, (2020).
3. Reading, H. G. *Sedimentary Environments: Processes, Facies and Stratigraphy* (3. Ed.). (Oxford: Blackwell Science, 1996).
4. Olsen, P. E., & Kent, D. V. Long-period Milankovitch cycles from the Late Triassic and Early Jurassic of eastern North America and their implications for the calibration of the Early Mesozoic time-scale and the long-term behaviour of the planets. *Philos. Trans. R. Soc. Lond., Series A: Mathematical, Physical and Engineering Sciences* **357(1757)**, 1761-1786 (1999).
5. Kemp, D. B., & Coe, A. L. A nonmarine record of eccentricity forcing through the Upper Triassic of southwest England and its correlation with the Newark Basin astronomically calibrated geomagnetic polarity time scale from North America. *Geology* **35(11)**, 991-994 (2007).
6. Vollmer, T. Orbital control on Upper Triassic Playa cycles of the Steinmergel-Keuper (Norian): A new concept for ancient playa cycles. *Palaeogeogr. Palaeoclimatol. Palaeoecol.* **267(1-2)**, 1-16 (2008).
7. Bahr, A. et al. Mega-monsoon variability during the late Triassic: Re-assessing the role of orbital forcing in the deposition of playa sediments in the Germanic Basin. *Sedimentology* **67(2)**, 951-970 (2020).
8. Rothwell, R. G. *Twenty years of XRF core scanning marine sediments: what do geochemical proxies tell us? Micro-XRF Studies of Sediment Cores.* (Springer, Dordrecht, 2015).
9. Rothwell, R. G., Hoogakker, B., Thomson, J., Croudace, I. W., & Frenz, M. Turbidite emplacement on the southern Balearic Abyssal Plain (western Mediterranean Sea) during Marine Isotope Stages 1–3: an application of ITRAX XRF scanning of sediment cores to lithostratigraphic analysis. *Geol. Soc. London, Spec. Publ.* **267(1)**, 79-98 (2006).
10. Zhang, S. et al. Orbital forcing of climate 1.4 billion years ago. *Proc. Natl. Acad. Sci. U.S.A.* **112(12)**, E1406-E1413 (2015).
11. Kodama, K. P., & Hinnov, L. A. *Rock magnetic cyclostratigraphy* (Vol. 5). (John Wiley & Sons, 2015).
12. Robinson, S. G. The late Pleistocene palaeoclimatic record of North Atlantic deep-sea sediments revealed by mineral-magnetic measurements. *Phys. Earth Planet.* **42(1-2)**, 22-47 (1986).
13. Thompson, R., Oldfield F. *Environmental Magnetism.* (Allen and Unwin, London, 1986)
14. Lepre, C. J., & Olsen, P. E. Hematite reconstruction of Late Triassic hydroclimate over the Colorado Plateau. *Proc. Natl. Acad. Sci. U.S.A.* **118(7)**, (2021).
15. Kemp, D. B. Optimizing significance testing of astronomical forcing in cyclostratigraphy. *Paleoceanography* **31(12)**, 1516-1531 (2016).
16. Sha, J. et al. Triassic–Jurassic climate in continental high-latitude Asia was dominated by obliquity-paced variations (Junggar Basin, Ürümqi, China). *Proc. Natl. Acad. Sci. U.S.A.* **112(12)**, 3624-3629 (2015).

17. Meyers, S. R. Cyclostratigraphy and the problem of astrochronologic testing. *Earth Sci. Rev.* **190**, 190-223 (2019).
18. Hajek, E. A., & Straub, K. M. Autogenic sedimentation in clastic stratigraphy. *Annu. Rev. Earth Planet. Sci.* **45**, 681-709 (2017).
19. Kim, W., & Paola, C. Long-period cyclic sedimentation with constant tectonic forcing in an experimental relay ramp. *Geology* **35(4)**, 331-334 (2007).
20. Kent, D. V., & Clemmensen, L. B. Paleomagnetism and cycle stratigraphy of the Triassic Fleming Fjord and Gipsdalen formations of East Greenland. *Bull. Geol. Soc. Denmark* **46**, 121–136 (1996).
21. Kent, D. V., & Clemmensen, L. B. Northward dispersal of dinosaurs from Gondwana to Greenland at the mid-Norian (215–212 Ma, Late Triassic) dip in atmospheric pCO<sub>2</sub>. *Proc. Natl. Acad. Sci. U.S.A.* **118(8)**, (2021).
22. Laskar, J., Fienga, A., Gastineau, M., & Manche, H. La2010: a new orbital solution for the long-term motion of the Earth. *Astron. Astrophys.* **532**, A89 (2011).
23. Laskar, J. et al. A long-term numerical solution for the insolation quantities of the Earth. *Astron. Astrophys.* **428(1)**, 261-285 (2004).
24. Kent, D. V. et al. Empirical evidence for stability of the 405-kiloyear Jupiter–Venus eccentricity cycle over hundreds of millions of years. *Proc. Natl. Acad. Sci. U.S.A.* **115(24)**, 6153-6158 (2018).
25. Olsen, P. E. et al. Mapping solar system chaos with the Geological Orrery. *Proc. Natl. Acad. Sci. U.S.A.* **116(22)**, 10664-10673 (2019).
26. Kent, D. V., Olsen, P. E., & Muttoni, G. Astrochronostratigraphic polarity time scale (APTS) for the Late Triassic and Early Jurassic from continental sediments and correlation with standard marine stages. *Earth Sci. Rev.* **166**, 153-180 (2017).
27. Guarnieri, P., Brethes, A., & Rasmussen, T. M. Geometry and kinematics of the Triassic rift basin in Jameson Land (East Greenland). *Tectonics* **36(4)**, 602-614 (2017).
28. Li, M. et al. Paleoclimate proxies for cyclostratigraphy: Comparative analysis using a Lower Triassic marine section in South China. *Earth Sci. Rev.* **189**, 125-146 (2019).
29. Kirschvink, J. L., The least-squares line and plane and the analysis of palaeomagnetic data, *Geophys. j. R. Astron. Soc.* **62**, 699-718 (1980).